Quasinormal modes, quasiperiodic oscillations, and the shadow of rotating regular black holes in nonminimally coupled Einstein-Yang-Mills theory

Kimet Jusufi,[1,2] Mustapha Azreg-Aïnou,[3] Mubasher Jamil,[4,5,6,7,*] Shao-Wen Wei,[8] Qiang Wu,[4,5] and Anzhong Wang[9]

[1]*Physics Department, State University of Tetovo, Ilinden Street nn, 1200, Tetovo, North Macedonia*
[2]*Institute of Physics, Faculty of Natural Sciences and Mathematics, Ss. Cyril and Methodius University, Arhimedova 3, 1000 Skopje, North Macedonia*
[3]*Başkent University, Engineering Faculty, Bağlıca Campus, 06790-Ankara, Turkey*
[4]*Institute for Theoretical Physics and Cosmology, Zhejiang University of Technology, Hangzhou 310023, China*
[5]*United Center for Gravitational Wave Physics, Zhejiang University of Technology, Hangzhou 310023, China*
[6]*Department of Mathematics, School of Natural Sciences (SNS), National University of Sciences and Technology (NUST), H-12, Islamabad, Pakistan*
[7]*Canadian Quantum Research Center 204-3002 32 Ave Vernon, British Columbia V1T 2L7, Canada*
[8]*Institute of Theoretical Physics & Research Center of Gravitation, Lanzhou University, Lanzhou 730000, China*
[9]*GCAP-CASPER, Physics Department, Baylor University, Waco, Texas 76798-7316, USA*

(Received 27 September 2020; accepted 11 November 2020; published 7 January 2021)

In this paper, we obtain an effective metric describing a regular and rotating magnetic black hole (BH) solution with a Yang-Mills electromagnetic source in Einstein-Yang-Mills (EYM) theory using the Newman-Janis (NJ) algorithm via the noncomplexification radial coordinate procedure. We then study the BH shadow and the quasinormal modes (QNMs) for massless scalar and electromagnetic fields and the quasiperiodic oscillations (QPOs). To this end, we also study the embedding diagram for the rotating EYM BH. The energy conditions, shadow curvature radius, topology, and the dynamical evolution of scalar and electromagnetic perturbations using the time domain integration method are investigated. We show that the shadow radius decreases by increasing the magnetic charge, while the real part of QNMs of scalar and electromagnetic fields increases by increasing the magnetic charge. This result is consistent with the inverse relation between the shadow radius and the real part of QNMs. In addition, we have studied observational constraints on the EYM parameter λ via frequency analysis of QPOs and the EHT data of shadow cast by the M87 central black hole. We also find that the decaying rate of the EYM BH is slower than that of the neutral and ends up with a tail. We argue that the rotating EYM black hole can be distinguished from the Kerr-Newman black hole with a magnetic charge based on the difference between the angular diameters of their shadows.

DOI: 10.1103/PhysRevD.103.024013

I. INTRODUCTION

It is generally believed that most of the giant elliptical and spiral galaxies contain supermassive black holes (SMBHs) at their galactic centers. For instance, the masses of SMBHs at the centers of Milky Way spiral galaxy and M87 elliptical galaxy are 4 million and 6 billion solar masses, respectively. Besides having huge masses, these SMBHs also possess spins (or angular momenta). Depending on the spacetime geometry, a black hole (BH) can capture light received from nearby stars or accretion disks into bound orbits. A large collection of light orbits constitutes a "photon sphere" around the BH. If the orbit of light is unstable, then photons (quanta of electromagnetic field) can either fall into the BH or escape to infinity (or a distant observer at a finite distance). The Event Horizon Telescope (EHT) Collaboration has detected the first shadow images of the SMBH at the center of the M87 galaxy [1,2]. With this image, it is observed that the diameter of the center BH shadow was approximately 52 μ-arc sec with a deviation of less than 10% from circularity, which leads to a measurement of the central mass of 6.5 billion solar mass. Importantly, these precise observations could provide a potential window to explore, distinguish, or constrain physically viable BH solutions

*Corresponding author.
mjamil@zjut.edu.cn

that exhibit small deviations from the Kerr metric. The distortion in the size and magnification of the shadow images provides information about the BH properties (such as its mass and spin) and the nearby geometry (the Schwarzschild, Kerr, or modified Kerr spacetime). Moreover, the shadow image is a manifestation of strong gravitational lensings, which can be used to distinguish various forms of BH spacetimes and naked singularities. Some of such studies on BH shadows in various gravitational theories were given in Refs. [3–9].

In the literature, numerous static and spherically symmetric BH solutions have been derived in the modified gravity theories (MGTs). However, the task of deriving the exact rotating black hole solutions analytically by solving the coupled field equations in any MGT has remained daunting due to the complexity of the nonlinear partial differential equations of the underlying theory. For instance, under reasonable assumptions of stationary, axial symmetry, and asymptotic flatness, the governing equations in f(R) gravity are highly nonlinear having the fourth-order derivatives, while in the general Horndeski theories, the field equations are second order. Still, one is able to generate the metrics of stationary and axis-symmetric BHs using the Newman-Janis algorithm (NJA) [10] and its modifications by starting with any seed static and spherically symmetric spacetime [11]. Among the modifications to NJA, there is the noncomplexification procedure of the radial coordinate [11]. This method has been extensively used in the literature for obtaining rotating BH solutions [12–36]. From the astrophysical and astronomical perspectives, almost all known candidates of BHs are rotating. The signature of rotation of a BH would be determined by the distortion of its shadow images or deviation from the spherical symmetry. The solution obtained by the NJA method is acceptable only if the resulting solution is free from geometrical pathologies and satisfies the energy conditions, causality, and regularity everywhere except at some spacetime singularities, while allowing the existence of a spatial hypersurface where a timelike Killing vector becomes null.

A rigorous proof about the existence of an infinite number of BH solutions to the Einstein-Yang-Mills (EYM) equations with the gauge group $SU(2)$ for any event horizon was provided in Ref. [37]. In the literature, slowly rotating non-Abelian BHs, numerical rotating BHs in the minimally coupled EYM theory, as well as nonstatic spherically symmetric EYM BHs were previously derived [38–41], in addition to the static, spherically symmetric constant curvature BHs [42]. Recently, new BH solutions have been also derived by adding Lorentz group symmetry in the minimally coupled EYM theory [43] and loop quantum corrections [44]. In this paper, we focus on the nonminimally coupled EYM theory where the curvature couples with the SU(2) gauge fields nontrivially [45,46]. Our aim is to test the nonminimally coupled EYM theory via constructing rotating BHs and then systematically investigate the consistency of the theory with the current and forthcoming observations, including the observations of M87 BH shadow. Furthermore, we would like to relate the shadow size with the quasinormal modes (QNMs) of the BHs. Here, gravitational waves will be treated as massless particles propagating along null geodesics and slowly leaking to infinity.

Among numerous astrophysical events, the quasiperiodic oscillations (QPOs) are very common phenomena in the x-ray power density spectra of stellar-mass BHs. The frequency of QPOs can be related to the matter orbiting in the vicinity of the innermost stable circular orbit (ISCO) of the BH. The appearance of two peaks at 300 and 450 Hz in the x-ray power density spectra of Galactic microquasars, representing possible occurrence of a lower QPO and of an upper QPO in a ratio of $3/2$, has stimulated a lot of theoretical works to explain the value of the $3/2$ ratio. Some theoretical models, including the parametric resonance, forced resonance, and Keplerian resonance, have been proposed. Therefore, the study of QPOs not only helps us understand the physical processes in BH mechanics but also provides a powerful approach to explore the nature of the BH spacetime in the strong field regime.

The structure of our paper is laid out as follows. In Sec. II, we review the nonminimally coupled EYM theory and the static BH solution. Henceforth, we apply the NJA modified by the noncomplexification procedure of the radial coordinate to generate the rotating counterpart of the static solution. In Secs. III and IV, we study the embedding diagram and energy conditions, respectively. In Secs. V and VI, we study the geometrical and astronomical features of the BH shadows and constraints on the free parameters. In Sec. VII, we investigate the curvature radius and its relation with the topology of the shadow. Section VIII is devoted to the investigation of QNMs of the static BH and their relationship with the radius of the shadow, as well as the dynamical evolution of scalar and electromagnetic perturbations. Section IX is devoted to QPOs and their resonances. First, we derive the generic expressions for the radial and vertical QPOs and then apply them to the rotating solution. In particular, we show how to obtain good and complete curve fits to the data of three microquasars. Finally, in Sec. X, we discuss our main results and provide some concluding remarks. There are also two Appendixes, in which we provide the exact expressions of the Einstein tensor and of some physical quantities pertaining to Sec. IX, respectively.

II. ROTATING REGULAR EINSTEIN-YANG-MILLS BH

Let us start by writing down the action of the nonminimally coupled EYM theory in four-dimensional spacetimes given by [45,46]

$$S=\frac{1}{8\pi}\int d^4x\sqrt{-g}\left[R+\frac{1}{2}F^{(a)}_{\mu\nu}F^{\mu\nu(a)}+\frac{1}{2}\mathcal{R}^{\alpha\beta\mu\nu}F^{(a)}_{\alpha\beta}F^{(a)}_{\mu\nu}\right], \tag{1}$$

in which g is the determinant of the metric tensor and R is the Ricci scalar. Furthermore, the greek indices run from 0 to 3, while the latin indices run from 1 to 3. On the other hand, the Yang-Mills (YM) tensor $F^{(a)}_{\mu\nu}$ is connected to the YM potential $A^{(a)}_{\mu}$ by the following relation:

$$F^{(a)}_{\mu\nu}=\nabla_\mu A^{(a)}_\nu-\nabla_\nu A^{(a)}_\mu+f^{(a)}_{(b)(c)}A^{(b)}_\mu A^{(c)}_\nu. \tag{2}$$

In the last equation, ∇_μ represents the covariant derivative, and $f^{(a)}_{(b)(c)}$ denote the real structure constants of the 3-parameters YM gauge group $SU(2)$. The tensor $\mathcal{R}^{\alpha\beta\mu\nu}$ is given by [46]

$$\begin{aligned}\mathcal{R}^{\alpha\beta\mu\nu}=&\frac{\xi_1}{2}(g^{\alpha\mu}g^{\beta\nu}-g^{\alpha\nu}g^{\beta\mu})\\&+\frac{\xi_2}{2}(R^{\alpha\mu}g^{\beta\nu}-R^{\alpha\nu}g^{\beta\mu}+R^{\beta\nu}g^{\alpha\mu}-R^{\beta\mu}g^{\alpha\nu})\\&+\xi_3R^{\alpha\beta\mu\nu},\end{aligned} \tag{3}$$

in which $R^{\alpha\beta}$ and $R^{\alpha\beta\mu\nu}$ are the Ricci and Riemann tensors, respectively. In addition, ξ_i $(i=1,\ 2,\ 3)$ are the nonminimally coupled parameters between the YM field and the gravitational field. With the assumptions that the gauge field is characterized by the Wu-Yang Ansatz and $\xi_1=-\xi$, $\xi_2=4\xi$, $\xi_3=-6\xi$ along with $\xi>0$, a regular, static, and spherically symmetric BH was found [45–47],

$$ds^2=-f(r)dt^2+\frac{dr^2}{g(r)}+h(r)(d\theta^2+\sin^2\theta d\phi^2), \tag{4}$$

with $f(r)=g(r)$, $h(r)=r^2$ and

$$g(r)=1+\left(\frac{r^4}{r^4+2\lambda}\right)\left(-\frac{2GM}{c^2r}+\frac{GQ^2}{4\pi\epsilon_0c^4r^2}\right). \tag{5}$$

Note that $\lambda=\xi Q^2$, while M is the BH mass and Q is the magnetic charge. When $\lambda=0$ and $Q=0$, the above metric reduces to the Schwarzschild BH. Furthermore, the total effective energy-momentum tensor consists of the pure Yang-Mills field and the effect of the coupling between the gravity and the Yang-Mills field [45,46]. From the Einstein field equation, the energy density and the radial and tangential pressures are derived as follows:

$$\begin{aligned}\rho=-p_r&=\frac{[Q^2(r^4-6\lambda)+16Mr\lambda]}{(r^4+2\lambda)^2},\\p_\theta=p_\phi&=\frac{Q^2(r^8-24\lambda r^4+12\lambda^2)-8M\lambda r(6\lambda-5r^4)}{(r^4+2\lambda)^3}.\end{aligned} \tag{6}$$

Now, we apply the modified NJ algorithm recently proposed in Ref. [11] to the static metric (4). The essence of the procedure is to drop the complexification of the r coordinate normally done in the NJ algorithm [10], as there does not exist a unique way to carry out it [11]. Dropping the complexification of r implies dropping the complexification of the metric functions $f(r)$, $g(r)$, and $h(r)$. Taking this advantage, Azreg-Aïnou replaced them by $F\equiv F(r,a,\theta)$, $G\equiv G(r,a,\theta)$, and $H\equiv H(r,a,\theta)$, respectively,

$$\begin{aligned}&f(r)\to F(r,a,\theta),\qquad g(r)\to G(r,a,\theta),\\&h(r)\to H(r,a,\theta).\end{aligned} \tag{7}$$

This combined algorithm should be called the NJAA algorithm or just NJAAA. Then, the remaining steps, as described in detail in Ref. [11], leads to the explicit expressions for F/H and GH,

$$\frac{F}{H}=\frac{gh+a^2\cos^2\theta}{[k(r)+a^2\cos^2\theta]^2},\qquad GH=gh+a^2\cos^2\theta, \tag{8}$$

where $k(r)\equiv\sqrt{g/f}h$, for which the rotating metric takes the form

$$\begin{aligned}ds^2=&-\frac{(g(r)h(r)+a^2\cos^2\theta)H}{(k(r)+a^2\cos^2\theta)^2}dt^2+\frac{Hdr^2}{g(r)h(r)+a^2}\\&-2a\sin^2\theta\left[\frac{k(r)-g(r)h(r)}{(k(r)+a^2\cos^2\theta)^2}\right]Hdtd\phi+Hd\theta^2\\&+H\sin^2\theta\left[a^2\sin^2\theta\left(\frac{2k(r)-g(r)h(r)+a^2\cos^2\theta}{(k(r)+a^2\cos^2\theta)^2}\right)\right.\\&\left.+1\right]d\phi^2.\end{aligned} \tag{9}$$

Now, since $f(r)=g(r)$, and $h(r)=r^2$, one finds $k(r)=h(r)=r^2$. Furthermore, the function $H(r,\theta,a)$ is still arbitrary and can be chosen so that the cross-term $G_{r\theta}$ of the Einstein tensor vanishes, i.e., $G_{r\theta}=0$, which yields the differential equation

$$(h(r)+a^2y^2)^2(3H_{,r}H_{,y^2}-2HH_{,ry^2})=3a^2h_{,r}H^2, \tag{10}$$

where $y\equiv\cos\theta$. It can be shown that the solution of the above equation takes the form [11]

$$H=\Sigma\equiv r^2+a^2\cos^2\theta. \tag{11}$$

Thus, summarizing all the above, the metric of the rotating BH finally reads

$$ds^2 = -c^2\left(1-\frac{2\Upsilon(r)r}{\Sigma}\right)dt^2 - 2ac\sin^2\theta\frac{2\Upsilon(r)r}{\Sigma}dtd\phi + \frac{\Sigma}{\Delta}dr^2 + \Sigma d\theta^2 + \frac{[(r^2+a^2)^2 - a^2\Delta\sin^2\theta]\sin^2\theta}{\Sigma}d\phi^2, \tag{12}$$

where

$$\Upsilon(r) = \frac{r(1-g(r))}{2}, \tag{13}$$

$$\Delta(r) = g(r)h(r) + a^2 = r^2 - \frac{r^6}{(r^4+2\lambda)}\left(\frac{2GM}{c^2 r} - \frac{GQ^2}{4\pi\epsilon_0 c^4 r^2}\right) + a^2. \tag{14}$$

The above metric is an effective metric describing a regular and rotating magnetic BH solution with a Yang-Mills electromagnetic source in the nonminimal Einstein-Yang-Mills theory. Metric (12) reduces to the Kerr-Newman BH with a magnetic charge instead of the electric charge if $\lambda = 0$. Thus, by continuity, it is certainly an exact solution to the field equations (Eq. (7) of Ref. [45]) at least for small λ. As we shall see in the subsequent sections, it is also free from geometrical pathologies and satisfies the energy conditions outside the outer horizon. In addition, it is free of spacetime singularity, too, as its curvature and Kretschmann scalar invariants are all regular for $\lambda > 0$,

$$R = \frac{8\lambda r^2[\mathcal{Q}^2(5r^4-6\lambda) + \mathcal{M}(-6r^5+20\lambda r)]}{(r^2+a^2\cos^2\theta)(r^4+2\lambda)^3}, \tag{15}$$

$$R^{\alpha\beta\mu\nu}R_{\alpha\beta\mu\nu} = \frac{P(r,\cos^2\theta,\mathcal{M},\mathcal{Q}^2,a^2,\lambda)}{(r^2+a^2\cos^2\theta)^6(r^4+2\lambda)^6}, \tag{16}$$

where P is a polynomial of its arguments and finite, $\mathcal{M} = GM/c^2$ and $\mathcal{Q}^2 = GQ^2/(4\pi\epsilon_0 c^4)$.

A. Effective energy-momentum tensor

In the NJAAA, the rotating solution is sourced by an anisotropic fluid the effective energy-momentum tensor $T^{\mu\nu}_{\text{eff}}$, which is diagonal in the orthonormal basis $(e_t, e_r, e_\theta, e_\phi)$ defined by [12,13]

$$e^\mu_t = \frac{(h+a^2,0,0,a)}{\sqrt{\Sigma\Delta}}, \qquad e^\mu_r = \frac{\sqrt{\Delta}(0,1,0,0)}{\sqrt{\Sigma}},$$
$$e^\mu_\theta = \frac{(0,0,1,0)}{\sqrt{\Sigma}}, \qquad e^\mu_\phi = \frac{(a\sin^2\theta,0,0,1)}{\sqrt{\Sigma}\sin\theta}. \tag{17}$$

Being given by the expression $T^{\mu\nu}_{\text{eff}} = \rho e^\mu_t e^\nu_t + p_r e^\mu_r e^\nu_r + p_\theta e^\mu_\theta e^\nu_\theta + p_\phi e^\mu_\phi e^\nu_\phi$, where ρ is the energy density and (p_r, p_θ, p_ϕ) are the components of the pressure, it can be shown that the effective energy-momentum tensor has the following components (examples of detailed calculations can be found in Refs. [12,13,22,23]):

$$\rho = -p_r = \frac{r^4[Q^2(r^4-6\lambda)+16Mr\lambda]}{(r^2+a^2\cos^2\theta)^2(r^4+2\lambda)^2},$$
$$p_\theta = p_\phi = \frac{r^2}{(r^2+a^2\cos^2\theta)^2(r^4+2\lambda)^3}\{8Mr\lambda[r^2(5r^4-6\lambda) + (3r^4-10\lambda)a^2\cos^2\theta] + Q^2[r^2(r^8-24\lambda r^4+12\lambda^2) - 4\lambda(5r^4-6\lambda)a^2\cos^2\theta]\}. \tag{18}$$

We can therefore say that rotating effective metric (12) is a solution to the field equation derived from the action given by Eq. (1) if all matter terms are replaced by the effective energy-momentum as defined in Eqs. (17) and (18). To have more elucidating expressions, we seek their Taylor

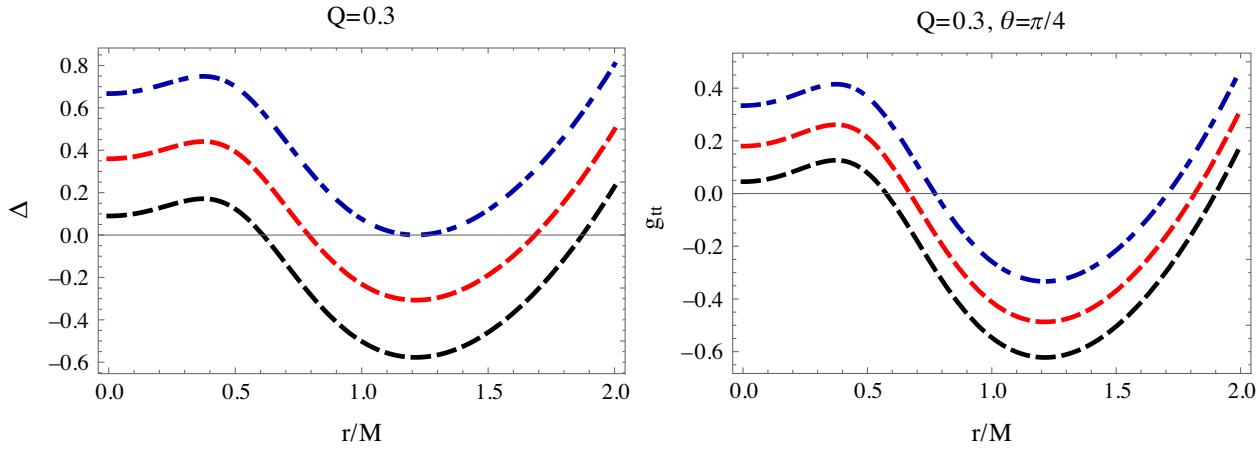

FIG. 1. Right panel: Variation of Δ as a function of r. For $Q = 0.3$, there is a critical value at $a = 0.817$ such that the horizon disappears. Left panel: Variation of g_{tt} as a function of r, with $\lambda = 0.1$. We choose $a = 0.3$ (black curve), $a = 0.6$ (red curve), and $a = 0.817$ (blue curve), in both plots.

expansions about $\lambda = 0$ in order to compare them with their counterparts of the Kerr-Newman black hole,

$$\rho = -p_r = \frac{Q^2}{(r^2 + a^2\cos^2\theta)^2} - \frac{2(5Q^2 - 8Mr)}{r^4(r^2 + a^2\cos^2\theta)^2}\lambda + \cdots,$$
$$p_\theta = p_\phi = \frac{Q^2}{(r^2 + a^2\cos^2\theta)^2} + \frac{1}{r^6(r^2 + a^2\cos^2\theta)^2}[8Mr(5r^2 + 3a^2\cos^2\theta) - 10Q^2(3r^2 + 2a^2\cos^2\theta)]\lambda + \cdots, \quad (19)$$

where the first term in each expression corresponds to the Kerr-Newman component of the energy-momentum tensor. We see clearly that the corrections added to the Kerr-Newman counterparts can be neglected, recalling that most observers are at large spatial distances from the sources. These corrections, proportional to λ, behave as the inverse of r^7 in the limit of large r, while the leading Kerr-Newman terms behave as the inverse of r^4.

We have discussed some relevant observable quantities, and there remain some other observable quantities, mainly the usual electromagnetic fields and their Yang-Mills extensions. In the literature, there are Ansätze [39] for

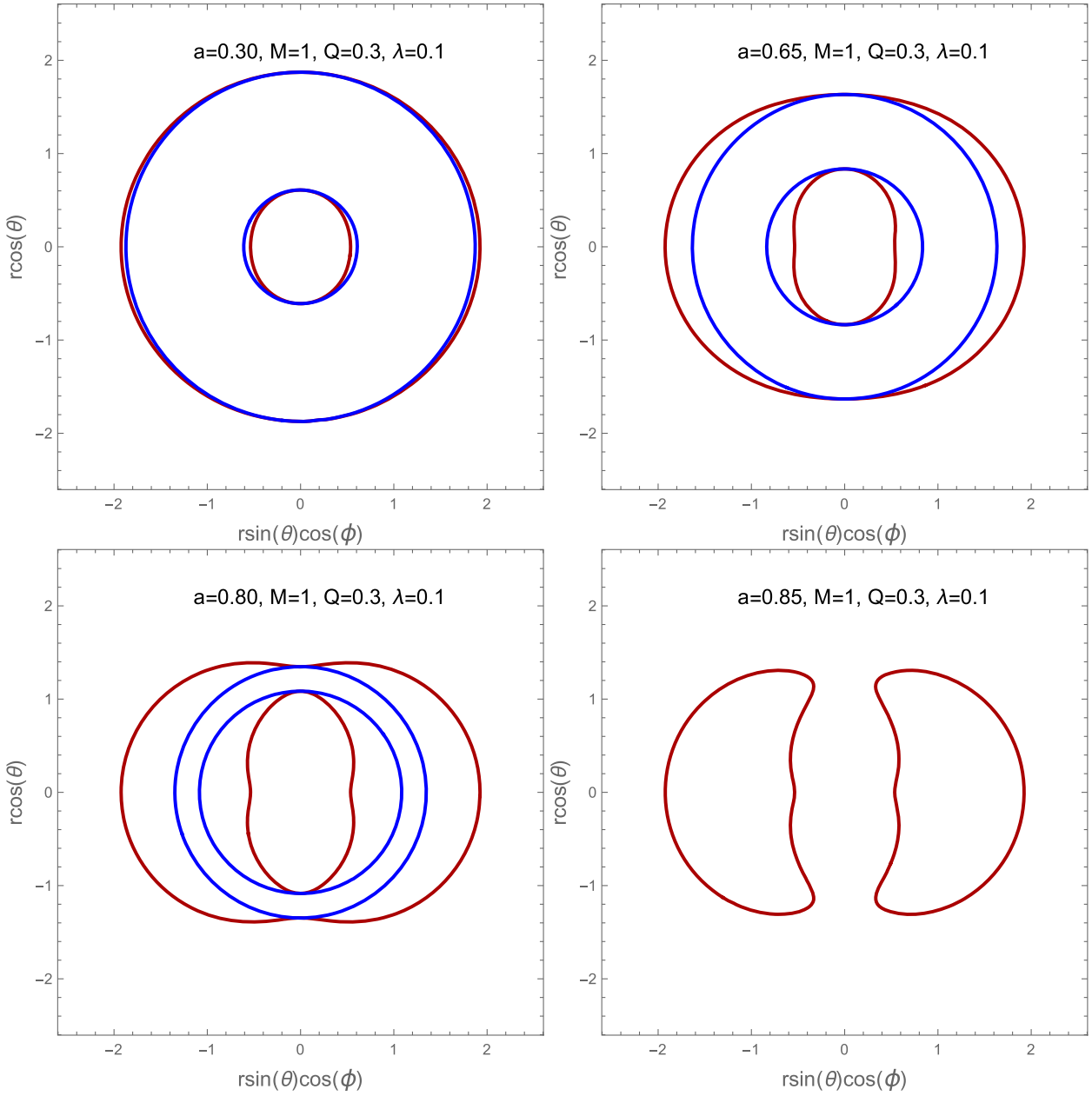

FIG. 2. Surface horizon (blue color) and ergoregion (red color) of the BH for different values of a. For $Q = 0.3$ and $a = 0.817$, we find that the horizon disappears. On the other hand, the magnetic charge has strong effects on the ergoregion surface.

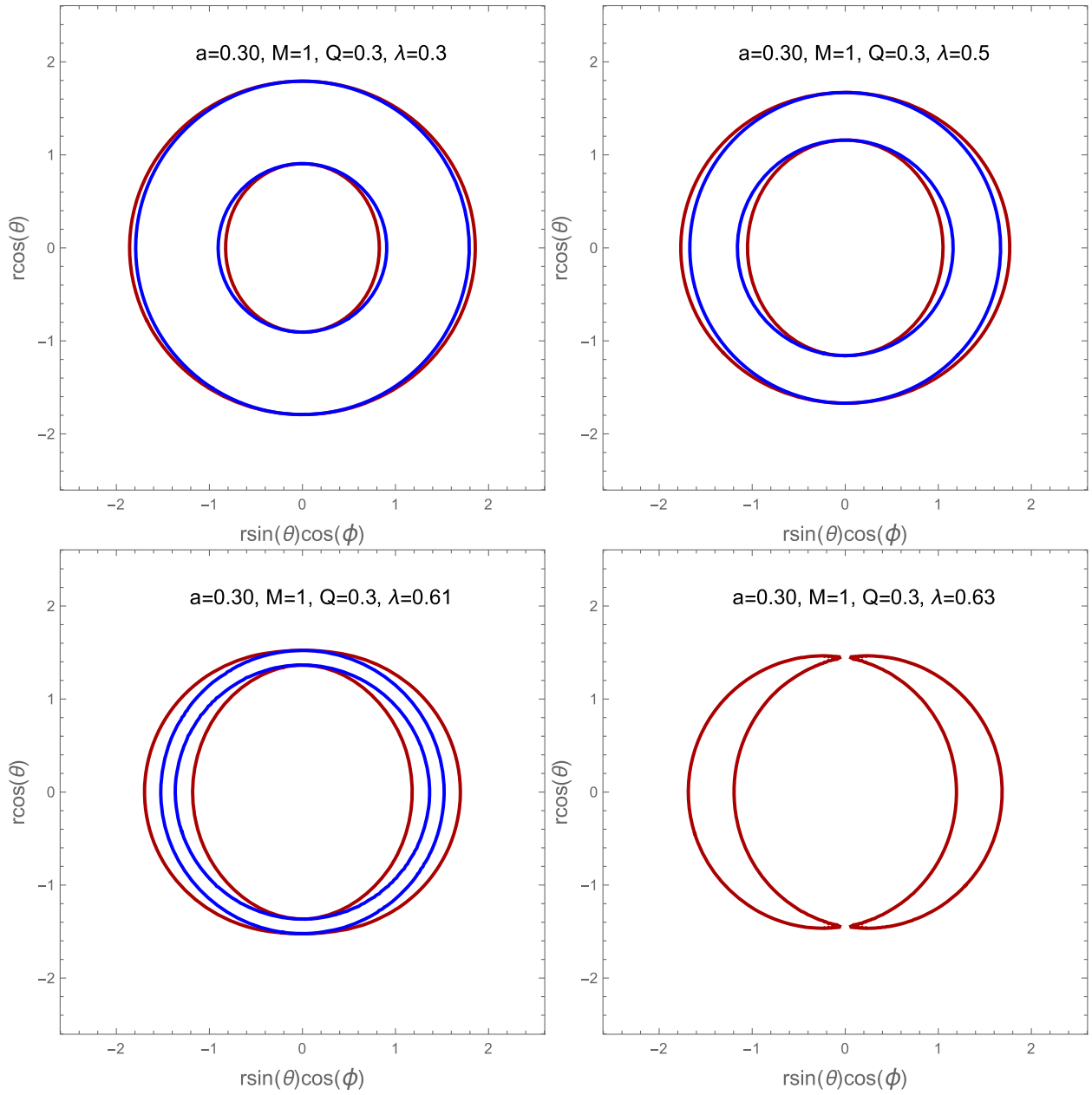

FIG. 3. Surface horizon (blue color) and ergoregion (red color) of the BH for different values of λ and fixed a and Q. For small values of λ, the black hole has two horizons, but if we increase λ, an extremal black hole is obtained, and the two horizons coincide. When $\lambda = 0.6225$, we find that the horizon disappears.

the general expressions of electromagnetic and Yang-Mills fields, but no exact analytical solutions were found; see, for example, Refs. [40,48,49] and references therein. The determination of the electromagnetic and Yang-Mills fields of the rotating black hole is more involved than the determination of the metric itself. This necessitates the resolution of coupled nonlinear differential equations and to the best of our knowledge only numerical solutions are available in the literature (see Refs. [40,48,49] and references therein). However, for our current purpose, such solutions are not needed.

B. Shape of the ergoregion

After obtaining the rotating BH solution (12), now let us turn to investigate its shape of the ergoregion. Usually, one plots the shape of the ergoregion in the xz-plane. The corresponding horizons of our BH can be found by solving the following equation $\Delta = 0$:

$$\Delta = g(r)h(r) + a^2 = 0. \tag{20}$$

In the meantime, the so-called static limit or ergosurface, inner and outer, is obtained via $g_{tt} = 0$, i.e.,

$$r^2 g(r) + a^2 \cos^2\theta = 0. \tag{21}$$

From Fig. 1, we observe that in general for a given Q and λ one gets two horizons if $a < a_c$. However, when $a = a_c$ (the blue line), the two horizons coincide, which means that we have an extremal BH with degenerate horizons. It is interesting to note that going beyond this critical value, $a > a_c$, one can see that event horizons no longer exist and the solution represents a compact object without horizons and singularities at the center. Moreover, by varying the angular momentum parameter a while having a constant value of magnetic charge, say, $Q = 0.3$, and a constant value of the parameter λ, say, $\lambda = 0.1$, one can see the effect of the magnetic charge on the surface horizon and ergoregion given in Fig. 2. For a given domain of parameters, we find that at certain value of the angular momentum $a = 0.817$ the horizon disappears. In Fig. 3, we depict the effect of the magnetic charge on the black hole horizons and ergoregions by varying the parameter λ, while having constant values of a and Q. It is shown that there is a domain of parameters and a critical value of λ_c such that the two horizons coincide, and for $\lambda > \lambda_c$, the horizons disappear.

III. EMBEDDING DIAGRAM

In this section, we investigate the geometry of the BH spacetime, by embedding it into a higher-dimensional Euclidean space. To this purpose, let us consider the equatorial plane $\theta = \pi/2$ at a fixed moment $t =$ Constant, for which the metric can be written as

$$ds^2 = \frac{dr^2}{1 - \frac{b(r)}{r}} + \mathcal{R}^2 d\phi^2, \tag{22}$$

where

$$b(r) = \frac{r^5}{(r^4 + 2\lambda)}\left(\frac{2M}{r} - \frac{Q^2}{r^2}\right) - \frac{a^2}{r}, \tag{23}$$

$$\mathcal{R}(r) = \left[r^2 + a^2 + \frac{a^2 r^4}{(r^4 + 2\lambda)}\left(\frac{2M}{r} - \frac{Q^2}{r^2}\right)\right]^{1/2}. \tag{24}$$

Let us embed this reduced BH metric into three-dimensional Euclidean space in the cylindrical coordinates,

$$ds^2 = dz^2 + d\mathcal{R}^2 + \mathcal{R}^2 d\phi^2 = \left[\left(\frac{d\mathcal{R}}{dr}\right)^2 + \left(\frac{dz}{dr}\right)^2\right] dr^2 + \mathcal{R}^2 d\phi^2. \tag{25}$$

From Eqs. (22) and (25), we find that

$$\frac{dz}{dr} = \pm\sqrt{\frac{r}{r - b(r)} - \left(\frac{d\mathcal{R}}{dr}\right)^2}, \tag{26}$$

where $b(r)$ is given by Eq. (23). Note that the integration of the last expression cannot be accomplished analytically. Invoking numerical techniques allows us to illustrate the embedding diagrams given in Fig. 4. It is seen that by varying the parameter λ the black hole geometry is significantly changed.

IV. ENERGY CONDITIONS

In this section, we are going to explore the energy conditions for the rotating EYM BH. For this purpose, we use the Einstein field equations $G_{\mu\nu} = 8\pi T_{\mu\nu}$ along with the effective energy-momentum tensor represented by a properly chosen tetrad of vectors given by $T^{\mu\nu} = e^{\mu}_{a} e^{\nu}_{b} T^{ab}$, where $T^{ab} = (\rho, p_r, p_\theta, p_\phi)$. In terms of the orthogonal basis, the nonvanishing components of the energy momentum tensor are given as follows [12]:

$$\rho = \frac{1}{8\pi} e^{\mu}_{t} e^{\nu}_{t} G_{\mu\nu}, \qquad p_r = \frac{1}{8\pi} e^{\mu}_{r} e^{\nu}_{r} G_{\mu\nu},$$
$$p_\theta = \frac{1}{8\pi} e^{\mu}_{\theta} e^{\nu}_{\theta} G_{\mu\nu}, \qquad p_\phi = \frac{1}{8\pi} e^{\mu}_{\phi} e^{\nu}_{\phi} G_{\mu\nu}. \tag{27}$$

The Einstein tensor $G_{\mu\nu}$ is given in Appendix A. Using the orthogonal bases given by Eq. (16), the corresponding physical quantities defined in Eq. (27) now read

$$\rho = -p_r = \frac{2\Upsilon'(r) r^2}{8\pi\Sigma^2},$$
$$p_\theta = p_\phi = p_r - \frac{\Upsilon''(r) r + 2\Upsilon'(r)}{8\pi\Sigma}. \tag{28}$$

In Fig. 5, by varying the parameter λ, we plot out the quantities ρ and $\rho + p_r + 2p$, where $p = p_\theta = p_\phi$, for a

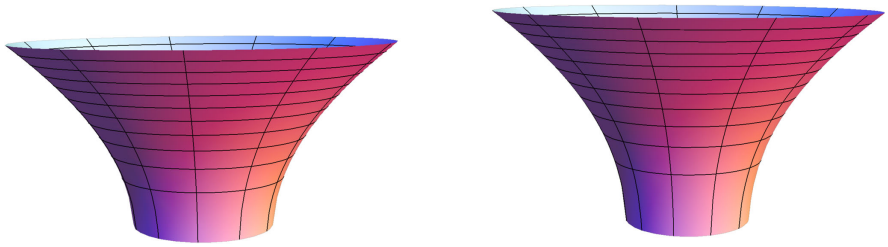

FIG. 4. The BH spacetime embedded in a three-dimensional Euclidean space. Left panel: we choose $a = 0.3$ and $\lambda = 0.1$. Right panel: we choose $a = 0.3$ and $\lambda = 0.5$. In both plots, we have used $M = 1$ along with $Q = 0.3$.

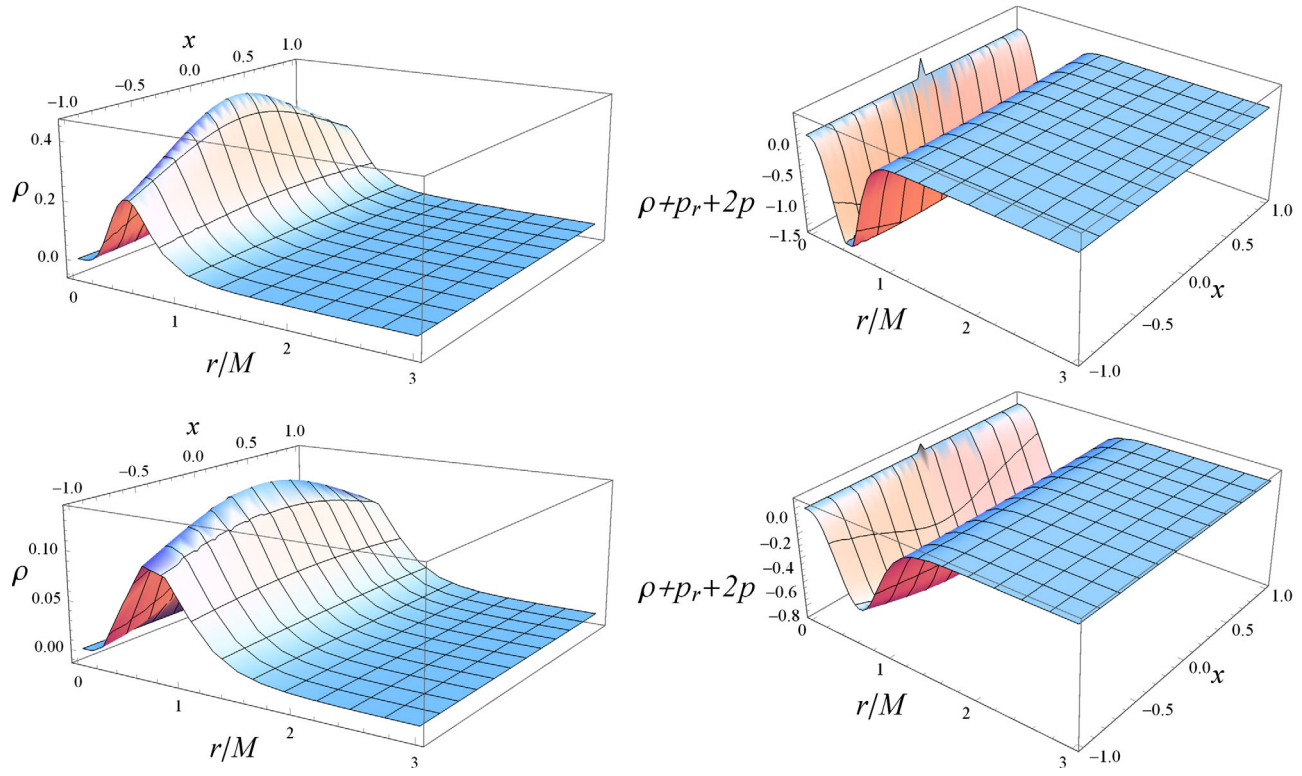

FIG. 5. Top left panel: plot of ρ with $\lambda = 0.1$ and $a = 0.3$. Top right panel: plot of $\rho + 2p_r + 2p$ with $\lambda = 0.1$ and $a = 0.3$. Bottom left panel: plot of ρ with $\lambda = 0.5$ and $a = 0.3$. Bottom right panel: plot of $\rho + 2p_r + 2p$ with $\lambda = 0.5$ and $a = 0.3$. Note that we have used $x = \cos\theta$ and set $M = 1$ along with $Q = 0.3$ in all the plots.

given values of (Q, a, M), from which we find that the strong energy condition (SEC) is not satisfied. In other words, the matter supporting this configuration is exotic, although we note that the cosmological constant does not satisfy the SEC either.

V. SHADOW OF THE ROTATING BHs

In order to find the contour of a BH shadow, we need to separate the null geodesic equations in the general rotating spacetime (12), by using the Hamilton-Jacobi equation given by

$$\frac{\partial \mathcal{S}}{\partial \sigma} = -\frac{1}{2} g^{\mu\nu} \frac{\partial \mathcal{S}}{\partial x^\mu} \frac{\partial \mathcal{S}}{\partial x^\nu}, \tag{29}$$

where σ is the affine parameter and $\mathcal{S}$ is the Jacobi action. In order to find a separable solution, we express the action in terms of the known constants of the motion as follows,

$$\mathcal{S} = \frac{1}{2}\mu^2 \sigma - Et + J\phi + \mathcal{S}_r(r) + \mathcal{S}_\theta(\theta), \tag{30}$$

where μ is the mass of the test particle, $E = -p_t$ is the conserved energy, and $J = p_\phi$ is the conserved angular momentum (with respect to the symmetry axis). For a photon, we have $\mu = 0$. From these equations, it is straightforward to obtain the following equations of motion (see, for instance, Ref. [11]),

$$\begin{aligned}
\Sigma \frac{dt}{d\sigma} &= \frac{r^2 + a^2}{\Delta}[E(r^2 + a^2) - aJ] - a(aE\sin^2\theta - J), \\
\Sigma \frac{d\phi}{d\sigma} &= \frac{a}{\Delta}[E(r^2 + a^2) - aJ] - \left(aE - \frac{J}{\sin^2\theta}\right), \\
\Sigma \frac{dr}{d\sigma} &= \pm\sqrt{\mathfrak{R}(r)}, \\
\Sigma \frac{d\theta}{d\sigma} &= \pm\sqrt{\Theta(\theta)},
\end{aligned} \tag{31}$$

where

$$\mathfrak{R}(r) = [X(r)E - aJ]^2 - \Delta(r)[\mathcal{K} + (J - aE)^2], \tag{32}$$

$$\Theta(\theta) = \mathcal{K} + a^2E^2\cos^2\theta - J^2\cot^2\theta \tag{33}$$

with $X(r) = (r^2 + a^2)$. The function $\Delta(r)$ is defined by Eq. (14), while $\mathcal{K}$ is the Carter separation constant. If we define the two quantities $\xi = J/E$ and $\eta = \mathcal{K}/E^2$ and make use the fact the unstable circular photon orbits in the general rotating spacetime must satisfy $\mathfrak{R}(r)(r_{\rm ph}) = 0$, $\mathfrak{R}(r)'(r_{\rm ph}) = 0$, and $\mathfrak{R}(r)'' \geq 0$, we obtain (see, for example, Ref. [36])

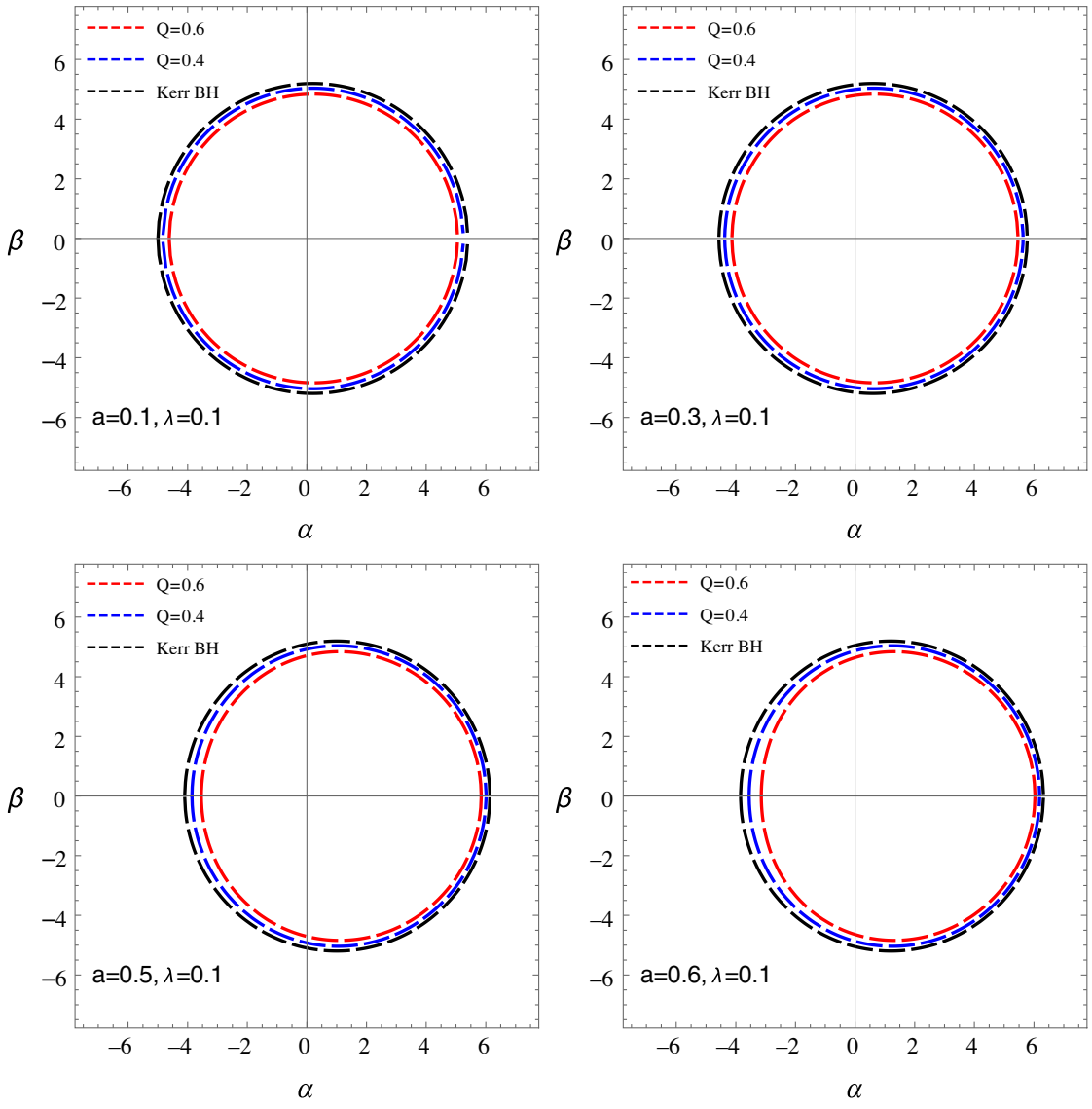

FIG. 6. Variation in the shape of the shadow of the rotating BH described by the metric (12) for different values of a and Q.

$$[X(r_{\rm ph}) - a\xi]^2 - \Delta(r_{\rm ph})[\eta + (\xi - a)^2] = 0, \quad (34)$$

$$2X'(r_{\rm ph})[X(r_{\rm ph}) - a\xi] - \Delta'(r_{\rm ph})[\eta + (\xi - a)^2] = 0, \quad (35)$$

where $r = r_{\rm ph}$ is the radius of the unstable photon orbit. Furthermore, if we eliminate η from the last two equations and then solve for ξ, we find that [36]

$$\xi = \frac{X_{\rm ph}\Delta'_{\rm ph} - 2\Delta_{\rm ph}X'_{\rm ph}}{a\Delta'_{\rm ph}}, \quad (36)$$

$$\eta = \frac{4a^2X'^2_{\rm ph}\Delta_{\rm ph} - [(X_{\rm ph} - a^2)\Delta'_{\rm ph} - 2X'_{\rm ph}\Delta_{\rm ph}]^2}{a^2\Delta'^2_{\rm ph}}, \quad (37)$$

where we note that the subscript "ph" indicates that the quantities are evaluated at $r = r_{\rm ph}$. Equations (36) and (37) give the general expressions for the critical impact parameters ξ and η of the unstable photon orbits, which describe the contour of the shadow.

The unstable photon orbits form the boundary of the shadow. The apparent shape of the shadow is obtained by using the celestial coordinates α and β, which lie in the celestial plane perpendicular to the line joining the observer and the center of the spacetime geometry. The coordinates α and β are defined by

$$\alpha = \lim_{r_0\to\infty}\left(-r_0^2 \sin\theta_0 \frac{d\phi}{dr}\bigg|_{(r_0,\theta_0)}\right), \quad (38)$$

$$\beta = \lim_{r_0\to\infty}\left(r_0^2 \frac{d\theta}{dr}\bigg|_{(r_0,\theta_0)}\right), \quad (39)$$

where (r_0, θ_0) are the position coordinates of the observer. After taking the limit, we obtain

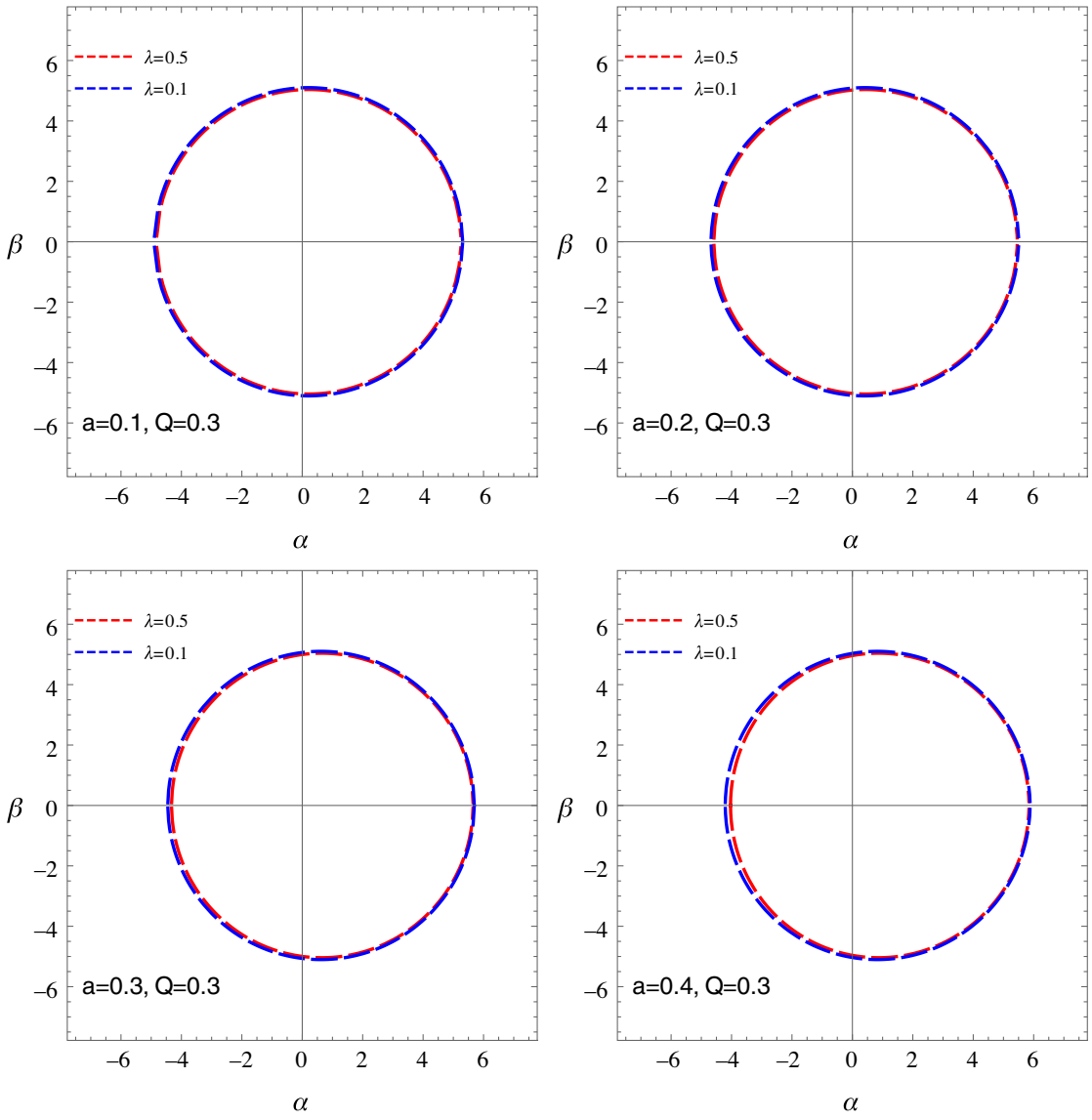

FIG. 7. Variation in the shape of the shadow of the rotating BH described by the metric (12) for different values of a and λ.

$$\alpha = -\frac{\xi}{\sin\theta_0}, \tag{40}$$

$$\beta = \pm\sqrt{\eta + a^2\cos^2\theta_0 - \xi^2\cot^2\theta_0}. \tag{41}$$

The shadow is constructed by using the unstable photon orbit radius $r_{\rm ph}$ as a parameter and then plotting out α and β using Eqs. (36), (37), (40), and (41). In Fig. 6, we show the effect of the magnetic charge by varying Q and a given values of (a, M, λ). It is observed that the black hole shadow radius decreases with the increase of Q. On the other hand, in Fig. 7, we show the effect of the magnetic charge by varying λ and a given values of (a, M, Q). It is observed that the black hole shadow radius monotonically decreases with the increase of λ, although the effect is very small compared to Fig. 6. Thus, for any $Q > 0$ and $\lambda > 0$, we see that the shadow radius is smaller compared to the Kerr-Newman black hole with a magnetic charge. As we see from Fig. 7, the effect of magnetic charge on the shadow radius is very small when we increase λ and, as a result, the EYM black hole is hard to distinguish from the Kerr-Newman black hole based on their shadows. The small effect of λ can be understood from the fact that if we consider a Taylor expansion of $g(r)$ around λ we obtain (working in natural units)

$$g(r) = 1 - \frac{2M}{r} + \frac{Q^2}{r^2} + \frac{2(2Mr - Q^2)\lambda}{r^6} + \cdots; \tag{42}$$

thus, the leading correction term behaves as the inverse of r^6. Despite the fact that the effect of λ is small, we are going to elaborate more on the possibility of distinguishing a rotating Kerr-Newman black hole with magnetic charge

TABLE I. Shadow radius of EYM black hole for different values of λ when viewed from the equatorial plane. In all these cases, we have set $M = 1$, $a = 0.2$, and $Q = 0.2$. Note that we have defined $\Delta\theta_s = \theta_s^{\rm KN} - \theta_s^{\rm EYM}$. For the Kerr-Newman black hole in terms of the above parameters, we have the typical shadow radius $\bar{R}_s^{\rm KN} = 5.149127296$ and an angular diameter $\theta_s^{\rm KN} = 39.33036448$ μ-arc sec, which corresponds to the case of $\lambda = 0$.

λ (M^4)	$\bar{R}_s^{\rm EYM}$ (M)	$\theta_s^{\rm EYM}$ (μ-arc sec)	$\Delta\theta_s$ (μ-arc sec)
0.1	5.134496817	39.21861310	0.11175138
0.2	5.119287867	39.10244321	0.22792127
0.3	5.103426195	38.98128766	0.34907682
0.4	5.086818521	38.85443395	0.47593053
0.5	5.069344363	38.72096183	0.60940265

from an EYM black hole based on the physical observable such as the shadow radius R_s and the angular diameter $\theta_s = 2R_sM/D$, where M is the black hole mass and D is the distance between the black hole and the observer. Our aim is to compute the shadow radius; however, in general, the shape of the shadow depends on the observer's viewing angle θ_0. In the present work, we are going to use an expression for the typical shadow radius of rotating black holes obtained by Jusufi [50],

$$\bar{R}_s = \frac{\sqrt{2}}{2}\left(\sqrt{\frac{r_0^+}{g'(r)|_{r_0^+}}} + \sqrt{\frac{r_0^-}{g'(r)|_{r_0^-}}}\right), \tag{43}$$

provided the black hole shadow is viewed from the equatorial plane. In addition, the radius of circular null geodesics $r_0^\pm$ for the prograde/retrograde orbit must be chosen such that both are outside of the horizon and can be obtained by solving the equation [50]

$$r_0^2 - \frac{2r_0}{g'(r)|_{r_0}} g(r_0) \mp 2a\sqrt{\frac{2r_0}{g'(r)|_{r_0}}} = 0. \tag{44}$$

In particular, we are going to use the M87 black hole with $M = 6.5 \times 10^9$ $M_{\odot)}$ and $D = 16.8$ Mpc. The angular diameter can be further expressed as $\theta_s = 2 \times 9.87098 \times 10^{-6} R_s(M/M_\odot)(1\ \text{kpc}/D)$ μ-arc sec. In Table I, we show the numerical values obtained for the typical shadow radius of a rotating EYM black hole by varying the parameter λ. From these numerical results, we can see that, as λ increases, the shadow radius and the corresponding angular diameter decrease, while the numerical values for the angular diameter are in the range 42 ± 3 μ-arc sec reported in Refs. [1,2]. In other words, as λ increases, it is easier to distinguish the EYM black hole from the Kerr-Newman black hole since the difference between their angular diameters given in terms of $\Delta\theta_s$ increases.

Now, we would like to study the observables of the shadow, which is useful for us to fit the observed data and determine the values of the black hole parameters.

Let us first introduce several characteristic points, the right point $(\alpha_r, 0)$, left point $(\alpha_l, 0)$, top point (α_t, β_t), and bottom point (α_b, β_b) of the shape. According to the symmetry of the shadow, one easily gets $\alpha_t = \alpha_b$ and $\beta_t = -\beta_b$. Following Ref. [51], we can construct the size and distortion of the shadow. The size of the shadow is described by the reference circle passing the top, bottom, and right points of the shadow. The reference circle cuts the α axis at $(\tilde{\alpha}_l, 0)$.

The radius of the reference circle can be calculated with these characteristic points,

$$R_s = \frac{(\alpha_t - \alpha_r)^2 + \beta_t^2}{2(\alpha_r - \alpha_t)}. \tag{45}$$

In the following, we will focus on two distortions δ_s and k_s, which can be defined as

$$\delta_s = \frac{\alpha_l - \tilde{\alpha}_l}{R_s}, \tag{46}$$

$$k_s = \frac{\beta_t - \beta_b}{\alpha_r - \alpha_l}. \tag{47}$$

For the nonrotating black hole, we can get $\delta_s = 0$ and $k_s = 1$, which means the shadow shape is a standard circle. However, when the black hole spin is nonzero, both these distortions deviate from these values.

In order to show how these two distortions vary with λ, we plot them in Fig. 8 for $Q = 0.4$ and $M = 1$. From the figures, we can find that for low spin the influence of λ on distortions δ_s and k_s is very tiny. δ_s and k_s almost keep 0 and 1, respectively. These indicates the shadow shapes are very close to standard circle. For $\theta_0 = \frac{\pi}{2}$, both δ_s and k_s increase with λ and approach to their maximal values for the extremal black holes. For example, when $a = 0.8$, the distortion δ_s takes 14%, and k_s takes 1.12, indicating the shadows have a big deformation from a standard circle. For $\theta_0 = \frac{\pi}{6}$, we find that the distortion k_s still increases with λ for different black hole spin. However, δ_s decreases, which is the result of the decrease in the shadow size. On the other sides, comparing with these figures, we can easily obtain the result that both the distortions get smaller with the decrease if θ_0. So, decreasing with θ_0, the shadows get less deformation.

In summary, if the observer is located near the equatorial plane, both the observables δ_s and k_s of the shadows increase with λ. If the observer is far off the equatorial plane, δ_s decreases, while k_s increases with λ. This provides us a possible way to test the magnetic black hole in EYM theory by making use of the shadows.

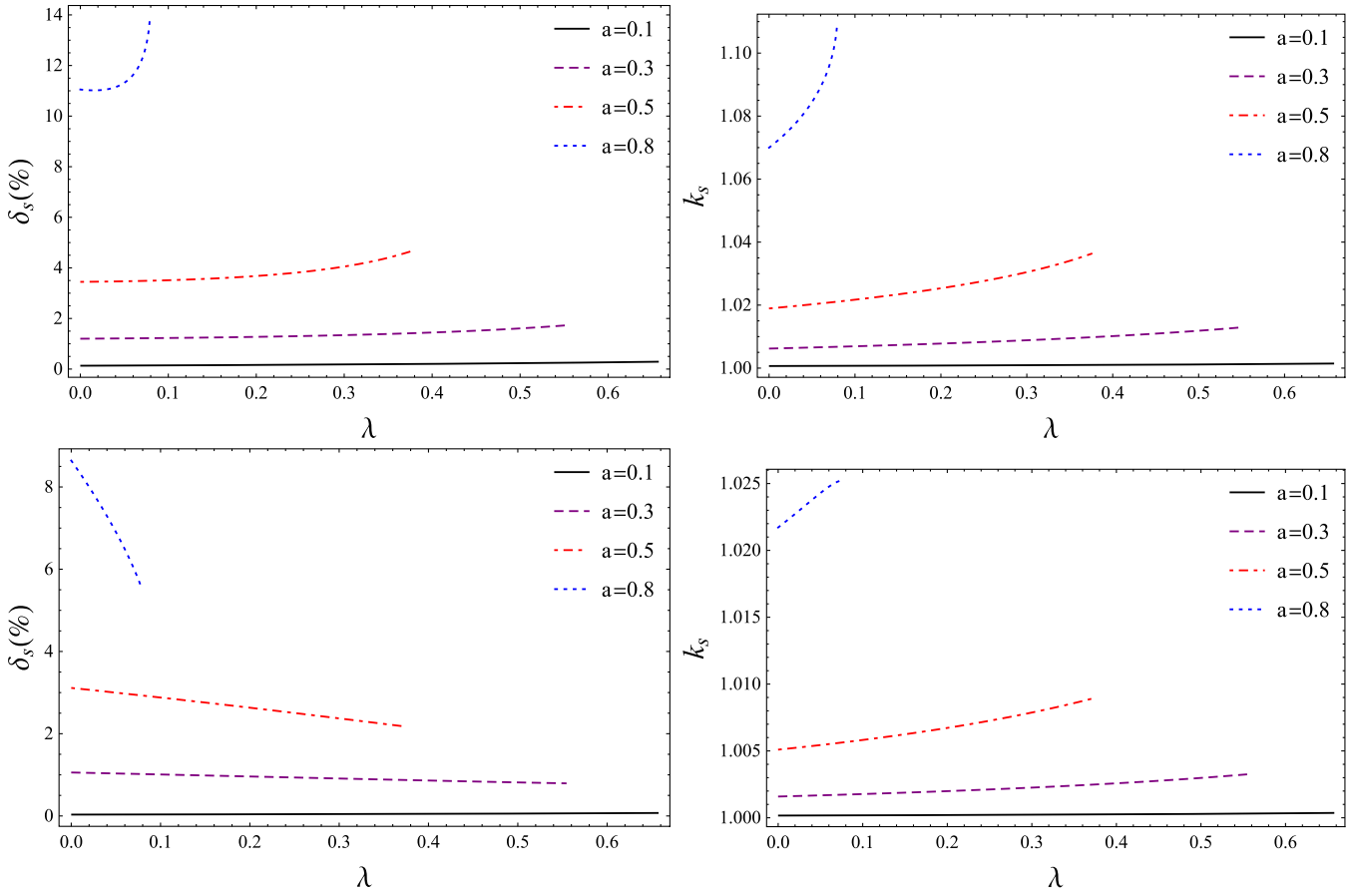

FIG. 8. Observables δ_s and k_s for $Q = 0.4$ and $M = 1$. The spin is set as $a = 0.1$, 0.3, 0.5, and 0.8 from bottom to top. In the top left and top right plots, we fixed $\theta = \pi/2$, whereas in the bottom left and bottom right figures, we used $\theta = \pi/6$.

VI. OBSERVATIONAL CONSTRAINTS

We can apply the numerical results of shadow size to the black hole of M87. The first M87 EHT results published the image of shadow of black hole with a ring diameter of 42 ± 3 μ-arc sec [1,2]. Adopting this measurement value and distance $D = 16.8 \pm 0.8$ Mpc, we performed the Monte Carlo simulations for the parameters space (M, Q, λ). The constraints on the parameter λ and mass of M87 are shown in Fig. 9. In 95% confidence level, the parameter λ is constrained as $\lambda = 0.53^{+0.93}_{-0.53}$, where we have applied the prior $\lambda > 0$. The mass of M87 is estimated as $M = (7.52^{+1.85}_{-1.56}) \times 10^9\ M_\odot$, which covers the range of value derived by EHT $M = (6.5 \pm 0.7) \times 10^9\ M_\odot$ in the Schwarzschild black hole. From above results, we found that there is a large parameter range to fit the EHT shadow size, so it is necessary to compare the above constraints with those obtained from other astrophysical observations.

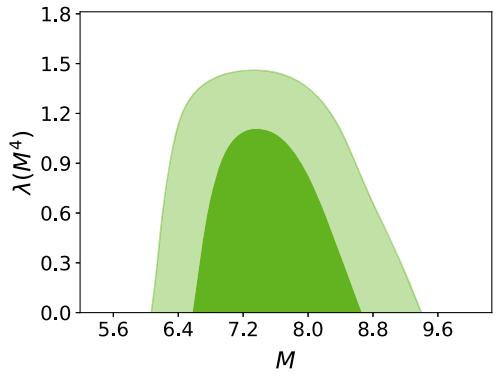

FIG. 9. Marginalized constrains for the parameter λ and estimated M87 black hole mass $M(\times 10^9\ M_\odot)$ using M87 shadow size in 68% and 95% confidence levels.

VII. CURVATURE RADIUS AND TOPOLOGY OF SHADOW

It is believed that the curvature radius has an important application in testing the BH shadow. Here, we aim to study the curvature radius and then discuss its topology following Refs. [52,53].

Since the curvature is parametrized by the length parameter, we first show the perimeter of the shadow. For a given shadow, its perimeter can be calculated with the following formula,

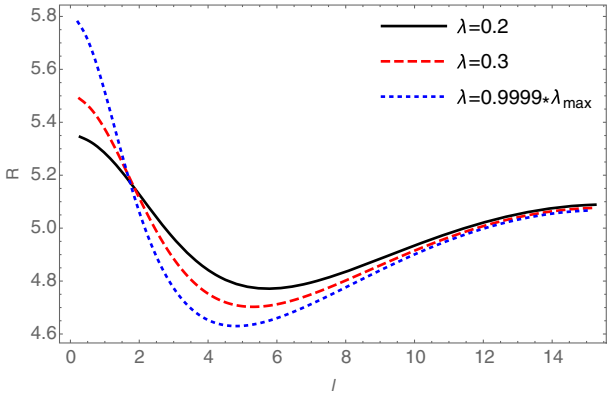

FIG. 10. Curvature radius as a function of the length parameter for $a = 0.5$, $Q = 0.4$, and $M = 1$. The parameter $\lambda = 0.2$, 0.3, and $0.9999 \times \lambda_{\max}$ with $\lambda_{\max} = 0.3752$.

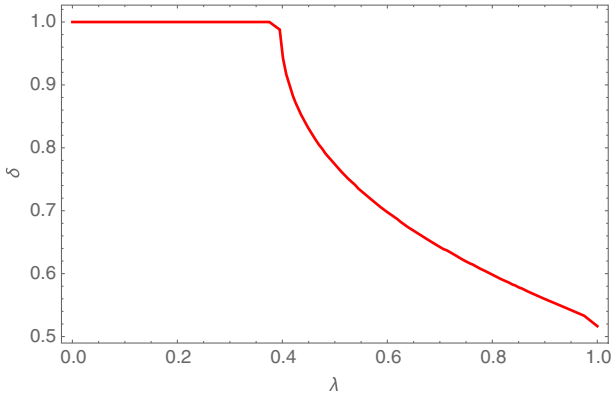

FIG. 11. Topological quantity δ as a function of λ for $a = 0.5$, $Q = 0.4$, and $M = 1$. For small λ, δ assumes the value 1, while for $\lambda > 0.3752$, δ decreases with λ.

$$l_s = 2\int \sqrt{(\partial_r \alpha)^2 + (\partial_r \beta)^2}\, dr, \tag{48}$$

where α and β are the celestial coordinates describing the shadow [52], as mentioned above. The factor 2 comes from the $\mathcal{Z}_2$ symmetry of the shadow. For $a = 0.5$, $Q = 0.4$, and $M = 1$, the perimeter l_s slightly decreases as λ increases (from 31.4936 to 30.9322 as λ varies from 0.01 to its maximum value 0.3752, corresponding to an extremal BH).

Since α and β are parametrized by r, we can adopt these forms to calculate the local curvature of the shadow R and l in terms of r as done in Refs. [52,53]. Finally, we plot R versus l in Fig. 10. In this plot, the first point on the perimeter of the shadow has the largest curvature value R, corresponding, by convention, to $l = 0$ (where l is the shadow segment length), and the last point corresponds to $l = l_s/2$, allowing us to drop the $\mathcal{Z}_2$ symmetry in the plot. We find that the curvature R first decreases with the length parameter l and then increases. This result is consistent with that of the Kerr BH shadows [52]. Along each curve, there is one maximum and one minimum. In particular, the maximum increases, while the minimum decreases with increasing the parameter λ.

When the shapes of the shadow are obtained from astronomical observations, we can use the curvature radius to fit the results and then obtain the values of the BH parameters. In Ref. [53], we discuss several different ways to determine the BH spin and the inclination angle of the observer for a Kerr BH. These provide possible applications on testing the nature of a BH through the shadow.

As we know, topology plays an important role in physics. In our investigation, topology can be used to describe differences between BHs and horizonless solutions [52]. To reveal the particular topological properties of the shadow, we introduce the topological covariant quantity [52],

$$\delta = \frac{1}{2\pi}\left(\int \frac{dl}{R} + \sum_i \theta_i\right). \tag{49}$$

Since in the current case the light ring is always unstable, the second term vanishes. Taking $a = 0.5$, $Q = 0.4$, and $M = 1$ as an example, we numerically calculate δ in terms of λ. The result is displayed in Fig. 11. From this figure, we see that, for small λ, δ assumes the value 1. While for $\lambda > 0.3752$, δ decreases, indicating a topological change corresponding to the transition from rotating BH to a rotating horizonless solution. Note that for $a = 0.5$, $Q = 0.4$, $M = 1$, and $\lambda < 0.3752$, the rotating solution is a BH with more than one horizon; for $\lambda = 0.3752$, it is an extremal BH; and for $\lambda > 0.3752$, it is a horizonless solution. This indicates a possible topological phase transition from a BH to a horizonless solution, a kind of gravitational vacuum condensate stars or gravastars without both an event horizon and a singularity at the center [54]. Gravastars are compact objects and may arise due to the Bose-Einstein condensation in gravitational systems resulting with an interior structure filled with vacuum energy and with an exterior effective Schwarzschild geometry if $a = 0$. So, the variation of λ indicates a change of the rotating solution from a BH to a compact object. Therefore, we conclude that the deviation from 1 of δ is a topological phase transition. The behavior of δ can act as a topological quantity to reflect the topological information of the spacetime structure.

VIII. CONNECTION BETWEEN THE SHADOW RADIUS AND QNMs

It is well known that QNMs in the eikonal regime are related to the angular velocity of the last circular null geodesic, while the imaginary part was related to the Lyapunov exponent, Λ, which determines the instability time scale of the orbit [55]. Then, the relation between QNMs and black hole lensing has been established by analyzing the photon sphere and light ring in a static spacetime or stationary spacetime, respectively [56–59]. However, it is convenient to express this connection in terms of the shadow radius and the real part of QNMs. Such a connection was obtained recently in Ref. [60] (see also Refs. [61,62]),

TABLE II. Numerical values for the shadow radius and the real part of QNMs obtained via Eq. (51). Here, we use a constant $\lambda = 0.1$ and change Q.

	$l=1,\ n=0$	$l=2,\ n=0$	$l=3,\ n=0$	
Q	$\omega_{\Re}$	$\omega_{\Re}$	$\omega_{\Re}$	R_S
0.1	0.2898919233	0.4831532055	0.6764144877	5.174342157
0.2	0.2913902646	0.4856504410	0.6799106174	5.147735467
0.3	0.2939658648	0.4899431080	0.6859203512	5.102633263
0.4	0.29774983241	0.4962497208	0.6947496090	5.037786211
0.5	0.3029582758	0.5049304598	0.7069026436	4.951176844

$$\omega_{\Re} = \lim_{l\gg 1} \frac{l}{R_S}. \tag{50}$$

This result was proved to be valid for the static spherical spacetime and accurate in the eikonal limit $l \gg 1$. Very recently, the correspondence between the shadow radius and the real part of QNMs frequencies was improved to the subleading regime to half of its value [63]

$$\omega_{\Re} = \lim_{l\gg 1} R_S^{-1}\left(l+\frac{1}{2}\right). \tag{51}$$

Of course, in the large angular momentum regime, i.e., $l \gg 1$, we recover Eq. (50). Thus, we can write

$$\omega_{\mathrm{QNM}} = \lim_{l\gg 1} R_S^{-1}\left(l+\frac{1}{2}\right) - i\left(n+\frac{1}{2}\right)|\Lambda|. \tag{52}$$

It is interesting to note that the above correspondence sometimes works well even for small values of l. It provides an alternative way to compute the real part of the QNMs by means of the shadow radius. In Tables II and III, we present the numerical calculations for the real part of QNMs obtained by means of the shadow radius. In the following, we are going to study the QNMs of scalar and electromagnetic fields in the spacetime of static EYM BH using the Wentzel-Kramers-Brillouin (WKB) method.

TABLE III. Numerical values for the shadow radius and the real part of QNMs obtained via Eq. (51). Here, we use a constant $Q = 0.3$ and change λ.

	$l=1,\ n=0$	$l=2,\ n=0$	$l=3,\ n=0$	
λ	$\omega_{\Re}$	$\omega_{\Re}$	$\omega_{\Re}$	R_S
0.0	0.2931522710	0.4885871182	0.6840219656	5.116794746
0.1	0.2939658648	0.4899431080	0.6859203512	5.102633264
0.2	0.2948115346	0.4913525578	0.6878935808	5.087996308
0.3	0.2956924989	0.4928208315	0.6899491641	5.072837511
0.4	0.2966125526	0.4943542542	0.6920959560	5.057102227

A. QNMs of a scalar field

Before we consider the problem of QNMs, let us point out that in this section we are going to simplify the problem by setting the rotation of the black hole to zero, i.e., $a = 0$. For the metric (4), we introduce the tortoise coordinate,

$$dr_\star = \frac{dr}{f(r)}, \tag{53}$$

in order to study perturbations of a massless scalar field, described by the equation

$$\frac{1}{\sqrt{-g}}\partial_\mu(\sqrt{-g}g^{\mu\nu}\partial_\mu\Phi) = 0. \tag{54}$$

Separation of variables of the function Φ in terms of the spherical harmonics yields

$$\Phi(t,r,\theta,\phi) = \frac{1}{r}e^{-i\omega t}Y_l(r,\theta)\Psi(r), \tag{55}$$

with $l = 0, 1, 2, \ldots$ being the multipole numbers. Then, one can show that the perturbations are governed by a Schrödinger wavelike equation,

$$\frac{d^2\Psi}{dr_\star^2} + (\omega^2 - V_S(r))\Psi = 0, \tag{56}$$

where the function Ψ satisfies the following boundary conditions,

$$\Psi(r_\star) = C_\pm \exp(\pm i\omega r_\star), \qquad r \to \pm\infty, \tag{57}$$

where ω can be written in terms of the real and imaginary parts, i.e., $\omega = \omega_{\Re} - i\omega_{\Im}$, where the imaginary part is proportional to the decay rate of a given mode. The effective potential $V_S(r)$ of the perturbations for the scalar field is given by

$$V_S(r) = \left[1 + \left(\frac{r^4}{r^4+2\lambda}\right)\left(-\frac{2M}{r}+\frac{Q^2}{r^2}\right)\right] \times \left[\frac{l(l+1)}{r^2} + \frac{2Mr^5 - 2Q^2r^4 - 12M\lambda r + 4Q^2\lambda}{(r^2+2\lambda)^2}\right]. \tag{58}$$

To solve Eqs. (56) and (58) with the boundary conditions (57), we use the WKB approximation to compute the quasinormal frequencies. The WKB method is widely used for numerical computations of QNMs and is based on the analogy with the problem of wave scattering near the peak of a potential barrier in quantum mechanics, where ω plays a role of energy [64,65]. In this work, we are going to use the sixth-order WKB

TABLE IV. The real and imaginary parts of the quasinormal frequencies of the scalar field with different values of Q. In all these cases, we have set $\lambda = 0.1$.

Spin 0	$l = 1$, $n = 0$	$l = 2$, $n = 0$	$l = 2$, $n = 1$
Q	ω(WKB)	ω(WKB)	ω(WKB)
0.1	0.2942-0.0968 i	0.4857-0.0958 i	0.4662-0.2924 i
0.2	0.2958-0.0969 i	0.4882-0.0959 i	0.4689-0.2927 i
0.3	0.2984-0.0971 i	0.4925-0.0961 i	0.4734-0.2932 i
0.4	0.3023-0.0972 i	0.4989-0.0963 i	0.4801-0.2937 i
0.5	0.3076-0.0974 i	0.5076-0.0965 i	0.4892-0.2941 i
0.6	0.3148-0.0974 i	0.5193-0.0966 i	0.5015-0.2940 i
0.7	0.3242-0.0969 i	0.5350-0.0963 i	0.5177-0.2927 i
0.8	0.3369-0.0954 i	0.5562-0.0950 i	0.5392-0.2883 i

approximation for calculating QNMs developed by Konoplya [66].

In Tables IV and V, we present the results for the scalar perturbations by varying the magnetic charge Q and the parameter λ, respectively. Note that we have not presented the calculations of QNMs for the fundamental mode $l = n = 0$ in Tables IV and V. This is simply related to the fact that the WKB method is applicable only when $l > n$ and does not give a satisfactory precision for this fundamental mode.

B. QNMs of an electromagnetic field

In this section, we precede to study the effect of the magnetic charge on the propagation of the electromagnetic field. To do so, we recall the wave equations for a test electromagnetic field,

$$\frac{1}{\sqrt{-g}}\partial_\nu[\sqrt{-g}g^{\alpha\mu}g^{\sigma\nu}(A_{\sigma,\alpha} - A_{\alpha,\sigma})] = 0. \tag{59}$$

The 4-potential A_μ can be expanded in terms of the four-dimensional vector spherical harmonics as

TABLE V. The real and imaginary parts of the quasinormal frequencies of the scalar field with different values of λ. In all these cases, we have set $Q = 0.3$.

Spin 0	$l = 1$, $n = 0$	$l = 2$, $n = 0$	$l = 2$, $n = 1$
λ	ω(WKB)	ω(WKB)	ω(WKB)
0.0	0.2975-0.0982 i	0.4912-0.0972 i	0.4717-0.2969 i
0.1	0.2984-0.0971 i	0.4925-0.0961 i	0.4734-0.2932 i
0.2	0.2993-0.0958 i	0.4939-0.0949 i	0.4749-0.2892 i
0.3	0.3001-0.0944 i	0.4953-0.0936 i	0.4762-0.2849 i
0.4	0.3008-0.0929 i	0.4967-0.0922 i	0.4771-0.2802 i
0.5	0.3013-0.0913 i	0.4980-0.0906 i	0.4776-0.2753 i
0.6	0.3016-0.0896 i	0.4994-0.0890 i	0.4774-0.2702 i
0.7	0.3018-0.0880 i	0.5006-0.0872 i	0.4767-0.2652 i

TABLE VI. The real and imaginary parts of the quasinormal frequencies of the electromagnetic field with different values of Q. In all these cases, we have set $\lambda = 0.1$.

Spin 1	$l = 1$, $n = 0$	$l = 2$, $n = 0$	$l = 2$, $n = 1$
Q	ω(WKB)	ω(WKB)	ω(WKB)
0.1	0.2501-0.0917 i	0.4598-0.0940 i	0.4392-0.2875 i
0.2	0.2515-0.0918 i	0.4623-0.0942 i	0.4418-0.2878 i
0.3	0.2541-0.0920 i	0.4665-0.0943 i	0.4464-0.2883 i
0.4	0.2579-0.0923 i	0.4728-0.0946 i	0.4530-0.2888 i
0.5	0.2631-0.0926 i	0.4815-0.0948 i	0.4621-0.2893 i
0.6	0.2702-0.0928 i	0.4931-0.0949 i	0.4744-0.2893 i
0.7	0.2798-0.0925 i	0.5088-0.0947 i	0.4907-0.2880 i
0.8	0.2928-0.0911 i	0.5301-0.0934 i	0.5126-0.2835 i

$$A_\mu(t,r,\theta,\phi) = \sum_{\ell,m}\left(\begin{bmatrix} 0 \\ 0 \\ \frac{a(t,r)}{\sin(\theta)}\partial_\phi Y_{\ell m}(\theta,\phi) \\ -a(t,r)\sin(\theta)\partial_\theta Y_{\ell m}(\theta,\phi) \end{bmatrix} + \begin{bmatrix} f(t,r)Y_{\ell m}(\theta,\phi) \\ h(t,r)Y_{\ell m}(\theta,\phi) \\ k(t,r)\partial_\theta Y_{\ell m}(\theta,\phi) \\ k(t,r)\partial_\varphi Y_{\ell m}(\theta,\phi) \end{bmatrix}\right), \tag{60}$$

in which $Y_{\ell m}(\theta,\phi)$ denotes the spherical harmonics. Without going into details, we find the following second-order differential equation for the radial part,

$$\frac{d^2\Psi(r_*)}{dr_*^2} + [\omega^2 - V_E(r_*)]\Psi(r_*) = 0, \tag{61}$$

with the effective potential

$$V_E(r) = \left[1 + \left(\frac{r^4}{r^4 + 2\lambda}\right)\left(-\frac{2M}{r} + \frac{Q^2}{r^2}\right)\right]\frac{l(l+1)}{r^2}. \tag{62}$$

In Tables VI and VII, we show the results for the electromagnetic perturbations by varying the magnetic charge

TABLE VII. The real and imaginary parts of the quasinormal frequencies of the electromagnetic field with different values of λ. In all these cases, we have set $Q = 0.3$.

Spin 1	$l = 1$, $n = 0$	$l = 2$, $n = 0$	$l = 2$, $n = 1$
λ	ω(WKB)	ω(WKB)	ω(WKB)
0.0	0.2526-0.0932 i	0.4650-0.0955 i	0.4443-0.2921 i
0.1	0.2541-0.0920 i	0.4665-0.0944 i	0.4464-0.2883 i
0.2	0.2556-0.0908 i	0.4681-0.0931 i	0.4482-0.2841 i
0.3	0.2570-0.0894 i	0.4697-0.0918 i	0.4499-0.2796 i
0.4	0.2583-0.0878 i	0.4713-0.0903 i	0.4512-0.2747 i
0.5	0.2594-0.0861 i	0.4729-0.0886 i	0.4521-0.2694 i
0.6	0.2602-0.0842 i	0.4745-0.0869 i	0.4522-0.2639 i
0.7	0.2606-0.0823 i	0.4760-0.0849 i	0.4516-0.2583 i

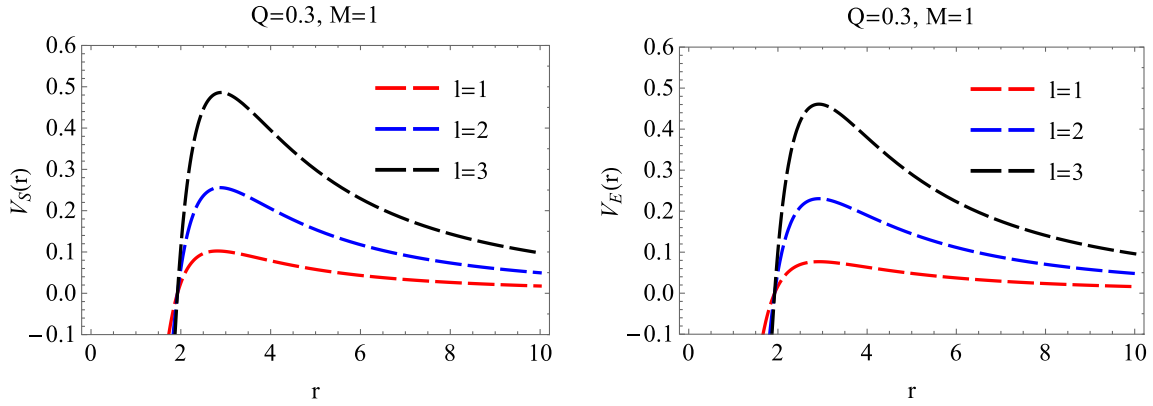

FIG. 12. Left panel: the effective potential of the scalar field for different values of l. Right panel: the effective potential of the electromagnetic field for different values of l.

Q and the parameter λ, respectively. From Fig. 12, we see that the effective potentials for both fields are indeed affected by the magnetic charge Q. From Fig. 13, we see that by increasing the magnetic charge Q, while having a constant λ, the real part of QNMs describing scalar and electromagnetic fields increases. A similar result is obtained when we increase the parameter λ while having a fixed value of Q; namely, the real part of QNMs increases monotonically, as can be seen in Fig. 14, although in this case, the effect of the magnetic charge on the real part of QNMs is smaller compared to the first case. From Tables IV–VII, it can also be seen that, in general, the absolute values of the imaginary part of QNMs decrease with the increase of the magnetic charge Q and λ, respectively. This means that the field perturbations in the spacetime of EYM black hole having $Q > 0$ or $\lambda > 0$ oscillate more rapidly compared to the vacuum Schwarzschild BH; however, in terms of damping, the field perturbations decay more slowly compared to the Schwarzschild BH. In addition to that, we see that for the scalar field perturbations the values of the real part of QNMs in absolute values are higher than those for the electromagnetic field perturbations (see Tables IV–VII). Thus, the scalar field perturbations will oscillate more rapidly compared to the electromagnetic field perturbations, in the same time the scalar field ones damp more rapidly than electromagnetic field ones. Once we compute the real part of QNMs and find that $\omega_{\Re}$ increases with Q with a constant λ, we can make use of the inverse relation between $\omega_{\Re}$ and the shadow radius R_S,

$$R_S(Q) = \lim_{l\gg 1} \frac{l+\frac{1}{2}}{\omega_{\Re}(Q)}\bigg|_{\lambda=\text{const}}, \tag{63}$$

which decreases with increasing Q as can be seen from Fig. 15 (left panel). This fact is verified in Fig. 6, where we have shown that the shadow radius decreases by increasing Q. Similarly, having the real part of QNMs with a varying λ and a constant Q, we can use

$$R_S(\lambda) = \lim_{l\gg 1} \frac{l+\frac{1}{2}}{\omega_{\Re}(\lambda)}\bigg|_{Q=\text{const}} \tag{64}$$

and show that the shadow radius monotonically decreases with increasing λ, as can be seen from Fig. 14 (right panel).

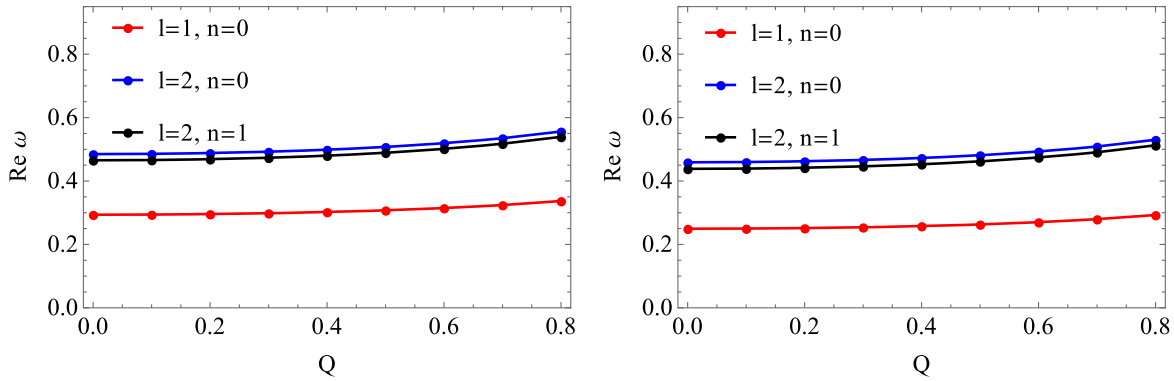

FIG. 13. Left panel: the real part of QNMs for the scalar field vs the magnetic charge Q. In both plots, we have set $\lambda = 0.1$. Right panel: the real part of QNMs for the electromagnetic field vs the magnetic charge Q. In both plots, we have set $\lambda = 0.1$.

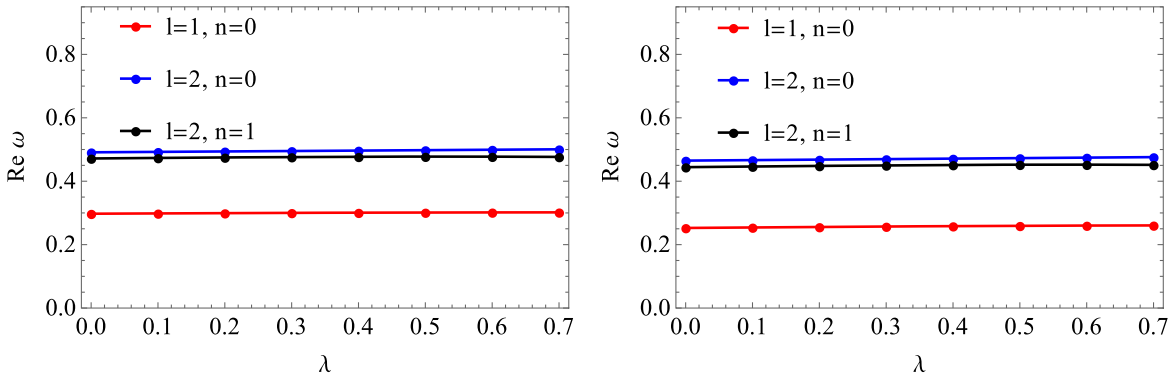

FIG. 14. Left panel: the real part of QNMs for the scalar field vs the parameter λ and constant magnetic charge $Q = 0.3$. Right panel: the real part of QNMs for the electromagnetic field vs the parameter λ and constant magnetic charge $Q = 0.3$.

This is consistent with Fig. 7, where we have shown that the shadow radius decreases by increasing λ. Finally, we can compare the numerical results for the real part of QNMs obtained from the shadow radius presented in Tables II and III with the ones obtained via the WKB method presented in Tables IV–VII. We observe that, even for the fundamental modes with small l, the accuracy between two methods works well for the case of the scalar field perturbations. Increasing l, the accuracy between the two methods increases.

C. Time domain integration method

Let us now explore the dynamical evolution of the scalar and electromagnetic perturbations using the time domain integration method. Toward this goal, first we simplify our computations by employing the following relation:

$$2M = f(r_h, \lambda, Q) = r_h + \frac{Q^2}{r_h} + \frac{2\lambda}{r_h^3}. \tag{65}$$

This means that we fix the mass of the BH and analyze when the line $y = 2M$ meets the curve $y = f(r_h, \lambda, Q)$ at the point of minimum. We call this mass the critical mass, $M = M_c$, and the horizon is denoted by $r = r_H$. In other words, the Cauchy and event horizons coincide. With that information in mind, we can rewrite Eq. (5) as follows [45]:

$$g(r) = \frac{(r - r_h)^2}{r^4 + 2\lambda}\left[r^2 + \frac{2\lambda}{r_h^2}\left(\frac{2r}{r_h} + 1\right)\right]. \tag{66}$$

Introducing the tortoise coordinate $r_\star = \int dr/g(r)$, we find that it is possible to write the wave equations (56) and (61) as follows,

$$\frac{\partial^2\Phi}{\partial r_\star^2} - \frac{\partial^2\Phi}{\partial t^2} = V_{S/E}(r)\Phi, \tag{67}$$

where $V_{S/E}(r)$ represents the effective potential for the scalar and electromagnetic field, respectively. One can determine the oscillation shape of the QNMs, by utilizing the finite difference method to study the dynamical evolution of the field perturbations in the time domain and examine the stability of the EYM BH. To do so, we first rewrite the wave equation in terms of the variables u and v,

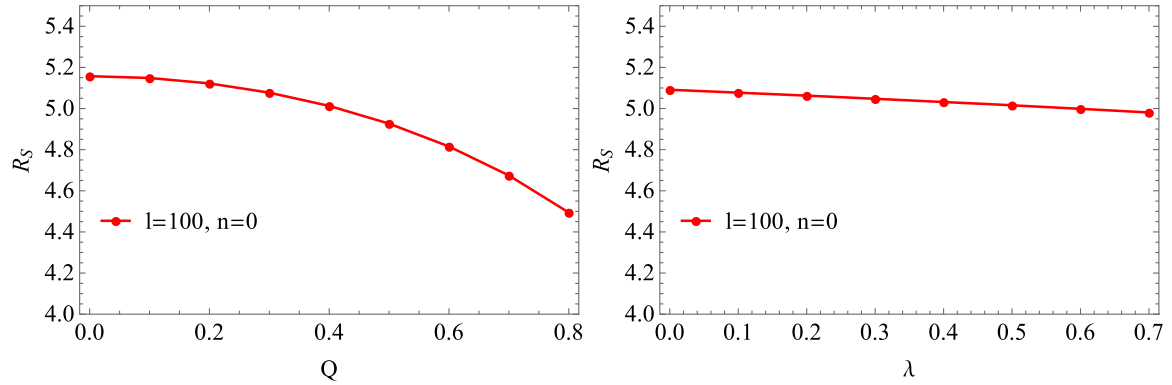

FIG. 15. Left panel: the plot of the shadow radius as a function of the magnetic charge Q obtained directly from the real part of QNMs given by Eq. (58). We have set $\lambda = 0.1$. Right panel: the plot of the shadow radius as a function of the parameter Q obtained from the real part of QNMs given by Eq. (59). We have set $Q = 0.3$.

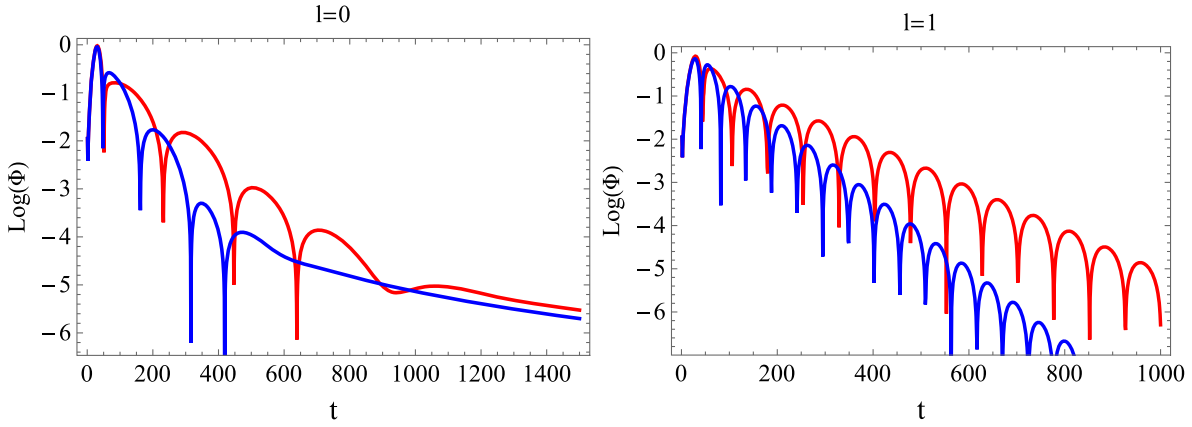

FIG. 16. The time domain profile for the scalar perturbations. Left panel: the red curve is the time domain profile for the EYM BH, and the blue curve is that for the Schwarzschild BH with $l = 0$. Right panel: the red curve is the time domain profile for the EYM BH, and the blue curve is that for the Schwarzschild BH with $l = 1$. We have set $\lambda = 0.1$ and $r_h = 1$ in both plots.

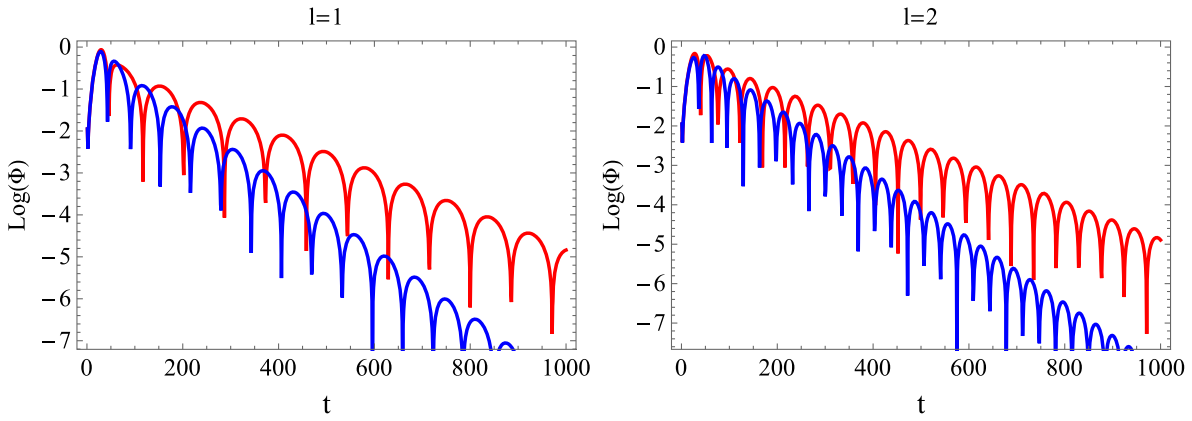

FIG. 17. The time domain profile for the electromagnetic perturbations. Left panel: the red curve is the time domain profile for the EYM BH, and the blue curve is that for the Schwarzschild BH with $l = 1$. Right panel: the red curve is the time domain profile for the EYM BH, and the blue curve is that for the Schwarzschild BH with $l = 2$. We have set $\lambda = 0.1$ and $r_h = 1$ in both plots.

$$\frac{\partial^2\Phi}{\partial u\partial v} + \frac{1}{4}V(r)\Phi = 0, \tag{68}$$

where $u = t - r_\star$ and $v = t + r_\star$, respectively. To solve this two-dimensional wave equation, we use a numerical method known as the finite difference method based on the following equation [67],

$$\Phi(u+\delta u, v+\delta v) = \Phi(u, v+\delta v) + \Phi(u+\delta u, v) - \Phi(u, v) - \delta u\delta v\Theta\frac{\Phi(u+\delta u, v) + \Phi(u, v+\delta u)}{8} + \mathcal{O}(\epsilon^4), \tag{69}$$

where

$$\Theta = V\left(\frac{2v - 2u + \delta v - \delta u}{4}\right). \tag{70}$$

Next, we suppose the initial perturbation as a Gaussian pulse, centered on v_c given by

$$\Phi(u = u_0, v) = e^{-\frac{(v-v_c)^2}{2\sigma^2}}. \tag{71}$$

With this initial condition, from Eqs. (69) and (70), we find numerically the function Φ and plot it out in Figs. 16 and 17 for different values of l. From these figures, we can see that the decaying rates of the scalar and electromagnetic perturbations in the EYM BH spacetime are slower than that of the Schwarzschild BH and end up in a tail. This conclusion is also supported by our numerical results obtained above by the WKB approximations.

IX. QUASIPERIODIC OSCILLATIONS (QPOs)

For the numerical calculations to be carried out in this section, we need the numerical values of some physical constants including the solar mass $M_\odot = 1.9888 \times 10^{30}$, the gravitational constant $G = 6.673 \times 10^{-11}$, and the speed of light in vacuum $c = 299792458$, all given in Systeme International units. These same constants will be

written explicitly in some subsequent formulas of this section.

In the power spectra of Fig. 3 of Ref. [68], we clearly see two peaks at 300 and 450 Hz, representing, respectively, the possible occurrence of the lower $\nu_L = 300$ Hz QPO and of the upper $\nu_U = 450$ Hz QPO from the Galactic microquasar GRO J1655-40. Similar peaks have been obtained for the microquasars XTE J1550-564 and GRS 1915 + 105 obeying the remarkable relation, $\nu_U/\nu_L = 3/2$ [69]. Some of the physical quantities of these three microquasars and their uncertainties are as follows [68,70],

$$\text{GRO J1655-40}: \quad \frac{M}{M_\odot} = 6.30 \pm 0.27, \quad \frac{a}{r_g} = 0.70 \pm 0.05$$
$$\nu_U = 450 \pm 3 \text{ Hz}, \quad \nu_L = 300 \pm 5 \text{ Hz}, \tag{72}$$

$$\text{XTE J1550-564}: \quad \frac{M}{M_\odot} = 9.1 \pm 0.6, \quad \frac{a}{r_g} = 0.405 \pm 0.115$$
$$\nu_U = 276 \pm 3 \text{ Hz}, \quad \nu_L = 184 \pm 5 \text{ Hz}, \tag{73}$$

$$\text{GRS } 1915 + 105: \quad \frac{M}{M_\odot} = 14.0 \pm 4.4, \quad \frac{a}{r_g} = 0.99 \pm 0.01$$
$$\nu_U = 168 \pm 3 \text{ Hz}, \quad \nu_L = 113 \pm 5 \text{ Hz}, \tag{74}$$

where $r_g \equiv GM/c^2$.

These twin values of the QPOs are most certainly due to the phenomenon of resonance which occurs in the vicinity of the ISCO, where the accreting particles perform radial and vertical oscillations around almost circular orbits. These two oscillations couple generally nonlinearly to yield resonances in the power spectra [71,72].

So, in the first part of this section, we will be concerned with stable circular orbits in the symmetry plane and their perturbations, since these orbits are mostly borrowed by infalling matter in accretion processes.

From now on, we consider stable circular orbits in the $\theta = \pi/2$ plane. First of all, we need to set up the equations governing an unperturbed circular motion. Once this is done, we will derive the equations that describe a perturbed circular motion around a stable unperturbed circular motion. In a third step, we will separate out the set of equations governing the perturbed circular motion.

The unperturbed circular motion is a geodesic motion obeying the equation

$$\frac{du^\mu}{d\tau} + \Gamma^\mu_{\alpha\beta} u^\alpha u^\beta = 0, \tag{75}$$

where $u^\mu = dx^\mu/d\tau = \dot{x}^\mu$ is the 4-velocity. Here, the connection $\Gamma^\mu_{\alpha\beta}$ is related to the unperturbed metric (12). For a circular motion in the equatorial plane ($\theta = \pi/2$), $u^\mu = (u^t, 0, 0, u^\phi) = u^t(1, 0, 0, \omega)$, where $\omega = d\phi/dt$ is the angular velocity of the test particle. The only equation describing such a motion is the r component of (75) and the normalization condition $g_{\mu\nu}u^\mu u^\nu = -c^2$, which take, respectively, the following forms,

$$\partial_r g_{tt}(u^t)^2 + 2\partial_r g_{t\phi} u^t u^\phi + \partial_r g_{\phi\phi}(u^\phi)^2 = 0, \tag{76}$$

$$g_{tt}(u^t)^2 + 2g_{t\phi}u^t u^\phi + g_{\phi\phi}(u^\phi)^2 = -c^2, \tag{77}$$

where the metric and its derivatives are evaluated at $\theta = \pi/2$. From them, we obtain

$$\omega = \frac{-\partial_r g_{t\phi} \pm \sqrt{(\partial_r g_{t\phi})^2 - \partial_r g_{tt}\partial_r g_{\phi\phi}}}{\partial_r g_{\phi\phi}},$$
$$u^t = \frac{c}{\sqrt{-(g_{tt} + 2\partial_r g_{t\phi}\omega + g_{\phi\phi}\omega^2)}},$$
$$u^\phi = \omega u^t, \tag{78}$$

where the upper sign corresponds to prograde circular orbits and the lower sign corresponds to retrograde orbits.

If the motion is perturbed, the actual position is now denoted by $X^\mu = x^\mu + \eta^\mu$ and the 4-velocity by $U^\mu = u^\mu + \dot{\eta}^\mu$ (where $\dot{} \equiv d/d\tau$) with u^μ being the unperturbed values given in (78). First, substituting it to

$$\frac{dU^\mu}{d\tau} + \Gamma^\mu_{\alpha\beta}(X^\sigma)U^\alpha U^\beta = 0, \tag{79}$$

where $\Gamma^\mu_{\alpha\beta}(X^\sigma)$ is the perturbed connection, and then keeping only linear terms in η^μ and its derivatives [and also considering (75)], we finally arrive at [73,74]

$$\ddot{\eta}^\mu + 2\Gamma^\mu_{\alpha\beta}u^\alpha\dot{\eta}^\beta + \partial_\nu\Gamma^\mu_{\alpha\beta}u^\alpha u^\beta\eta^\nu = 0, \tag{80}$$

where the background connection $\Gamma^\mu_{\alpha\beta}$ and its derivatives are all evaluated at $\theta = \pi/2$. As shown in Ref. [74], Eqs. (80) decouple and take the form of oscillating radial (in the $\theta = \pi/2$ plane) and vertical (perpendicular to the $\theta = \pi/2$ plane) motions obeying the following harmonic equations:

$$\ddot{\eta}^r + \Omega_r^2\eta^r = 0, \qquad \ddot{\eta}^\theta + \Omega_\theta^2\eta^\theta = 0. \tag{81}$$

The locally measured frequencies (Ω_r, Ω_θ) are related to the spatially remote observer's frequencies (ν_r, ν_θ) by

$$\nu_r = \frac{1}{2\pi}\frac{1}{u^t}\Omega_r, \qquad \nu_\theta = \frac{1}{2\pi}\frac{1}{u^t}\Omega_\theta, \tag{82}$$

where u^t is given in (78) and furthermore the frequencies are defined as [74]

$$\Omega_\theta^2 \equiv (\partial_\theta \Gamma^\theta_{ij}) u^i u^j, \qquad (i,j = t,\phi), \tag{83}$$

$$\Omega_r^2 \equiv (\partial_r \Gamma^r_{ij} - 4\Gamma^r_{ik}\Gamma^k_{rj}) u^i u^j, \qquad (i,j,k = t,\phi). \tag{84}$$

In these expressions, the summations extend over (t,ϕ). It is understood that all the functions appearing in (78), (82), and (83) are evaluated at $\theta = \pi/2$.

In terms of

$$x \equiv \frac{r}{r_g}, \qquad a_0 \equiv \frac{a}{r_g}, \qquad \lambda_0 \equiv \frac{\lambda}{r_g^4}, \qquad r_g \equiv \frac{GM}{c^2}, \tag{85}$$

the expressions of (ν_r, ν_θ) measured in hertz take the form

$$\nu_r = \frac{c^3}{2\pi GM}\sqrt{N}\sqrt{\frac{N_r}{D_r}}, \qquad \nu_\theta = \frac{c^3}{2\pi GM}\sqrt{N}\sqrt{\frac{N_\theta}{D_\theta}}, \tag{86}$$

where $(N, N_r, D_r, N_\theta, D_\theta)$ are given in Appendix B.

As we mentioned earlier, the twin values of the QPOs observed in the microquasars are most certainly due to the phenomenon of resonance resulting from the coupling of the vertical and radial oscillatory motions [71,72]. The most common models for resonances are parametric resonance, forced resonance, and Keplerian resonance. It is the general belief that the resonance observed in the three microquasars (72), (73), and (74) is of the nature of the parametric resonance and is given by

$$\nu_U = \nu_\theta, \qquad \nu_L = \nu_r, \tag{87}$$

with

$$\frac{\nu_\theta}{\nu_r} = \frac{n}{2}, \quad n \in \mathbb{N}^+. \tag{88}$$

In numerous applications of the parametric resonance, one usually considers the case $n = 1$ [75–78]. In such a case, ν_r is the natural frequency of the system and ν_θ is the parametric excitation ($T_\theta = 2T_r$, the corresponding periods), that is, the vertical oscillations supply energy to the radial oscillations causing resonance [78]. However, since $\nu_\theta > \nu_r$ in the vicinity of ISCO, where accretion occurs and QPO resonance effects take place, the lower possible value of n is 3, and in this case ν_r becomes the parametric excitation that supplies energy to the vertical oscillations.

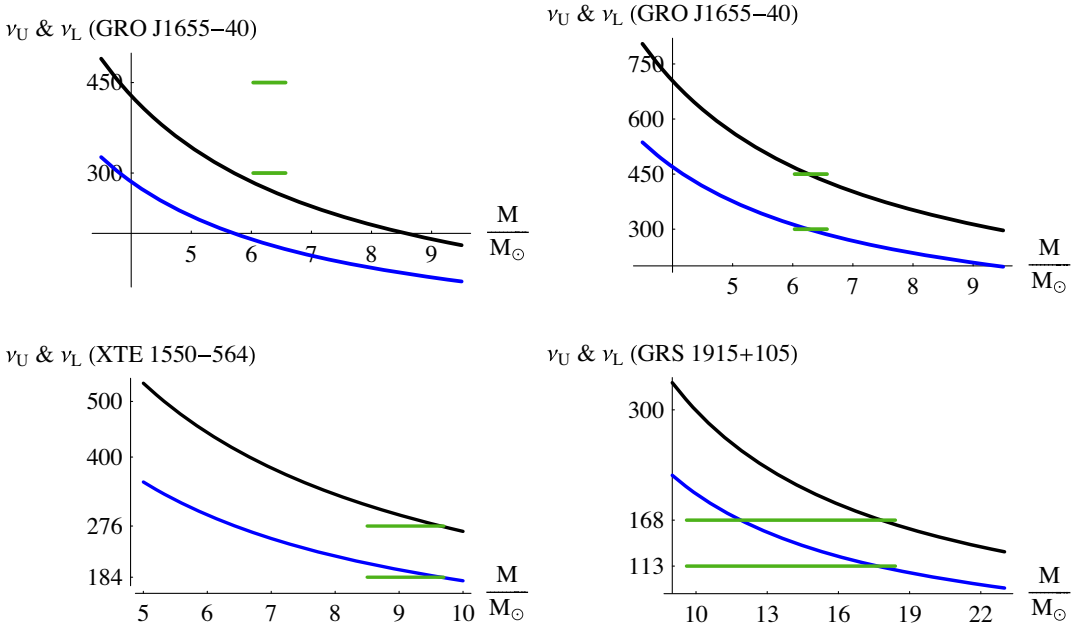

FIG. 18. Fitting the uncharged particle oscillation upper and lower frequencies to the observed frequencies (in hertz) for the microquasars GRO J1655-40, XTE J1550-564, and GRS 1915 + 105 at the 3/2 resonance radius. In these plots, each microquasar is treated as a rotating EYM BH given by Eq. (12) with $Q = 0$. The black curves represent $\nu_U = \nu_\theta$, the blue curves represent $\nu_L = \nu_r$ with $\nu_U/\nu_L = 3/2$, and the green curves represent the mass limits as given in (72), (73), and (74). Upper left panel: the microquasar GRO J1655-40 treated as a Kerr BH with $M/M_\odot = 6.3$ and $a/r_g = 0.70$ ($r_g \equiv GM/c^2$). We see that the black (blue) curve does not cross the upper (lower) mass error band. This panel has been added for comparison. Upper right panel: the microquasar GRO J1655-40 treated as a rotating EYM BH with $M/M_\odot = 6.3$, $a/r_g = 0.70$, and $\lambda/r_g^4 = 2.14$. We see that the black (blue) curve crosses the upper (lower) mass error band. Lower left panel: the microquasar XTE J1550-564 treated as a rotating EYM BH with $M/M_\odot = 9.1$, $a/r_g = 0.51$, and $\lambda/r_g^4 = 4.30$. The black (blue) curve crosses the upper (lower) mass error band. Lower right panel: the microquasar GRS 1915 + 105 treated as a rotating EYM BH with $M/M_\odot = 9.7$, $a/r_g = 0.99$, and $\lambda/r_g^4 = 0.005$. The black (blue) curve crosses the upper (lower) mass error band.

Thus, the observed ratio $\nu_U/\nu_L = 3/2$ is theoretically justified by making the assumptions (87) and (88) with $n = 3$. Numerically, we have to show that the plot of ν_θ (ν_r) versus $M/M_\odot$ crosses the upper (lower) mass band error, given in (72), (73), and (74), as a_0 assumes values in its defined band error and $\lambda_0 > 0$ runs within some interval to be defined later as the interval of its constrained values.

Curves that fit the upper and lower oscillation frequencies of the uncharged test particles to the observed frequencies (in hertz) of the microquasars GRO J1655-40, XTE J1550-564, and GRS $1915 + 105$ at the $3/2$ resonance radius are presented in Fig. 18. In these plots, each microquasar is treated as a rotating EYM BH (12) with $Q = 0$. The black curves represent $\nu_U = \nu_\theta$ versus $M/M_\odot$, the blue curves represent $\nu_L = \nu_r$ versus $M/M_\odot$ with $\nu_U/\nu_L = 3/2$, and the green curves represent the mass limits as given in (72), (73), and (74). For comparison, we start with the upper left panel where the microquasar GRO J1655-40 is treated as a Kerr BH ($\lambda_0 = 0$) with $M/M_\odot = 6.3$ and $a/r_g = 0.70$. We see that the black (blue) curve does not cross the upper (lower) mass error band. In the other remaining three panels, where each microquasar is treated as a rotating EYM BH (12), we see how the black (blue) curve crosses the upper (lower) mass error band for each of the microquasars. The curve fittings allow us to fix the following limits for λ_0:

$$0 < \lambda_0 \lesssim 4.3. \tag{89}$$

It is worth noting that the ratio $\nu_U/\nu_L = 3/2$ may sometimes admit two x roots. In our plot, we have chosen the root that is closer to $x_{\rm ISCO}$ where the events of accretion and QPOs occur.

For completeness and comparison, two other plots (not shown in this paper) similar to those in the upper left panel of Fig. 18 have been sketched for the microquasars XTE J1550-564 and GRS $1915 + 105$ treating them as the Kerr BH ($\lambda_0 = 0$). For the microquasar XTE J1550-564, the plots show no intersections of the curves (ν_U, ν_L) with the mass error bands, and for the microquasar GRS $1915 + 105$, intersections exist, but these are certainly due to the large mass band error for this microquasar (74).

Other curves that fit the data of the three microquasars (72), (73), and (74) have been given either via the immersion of a Schwarzschild BH into a test magnetic field [79] or via the consideration of generalized theories of gravity [80].

X. CONCLUSION

In this paper, we have obtained a rotating regular magnetic BH solution of the EYM theory, by applying the NJAAA to a spherical symmetric solution. We have then investigated the ergosurface and the BH shadow. We have found that the magnetic charge Q causes deformations to both the size and shape of the BH shadow. For a given value of the angular momentum a and the inclination angle θ_0, the presence of the magnetic charge Q shrinks the shadow and enhances its deformation with respect to the shadow of the Kerr spacetime. In other words, the shadow radius decreases due to the presence of the magnetic charge Q. Among other things, we have constructed the embedding diagram for the rotating EYM BH and examined the energy conditions. In particular, it has been found that the strong energy condition in general is not satisfied. The particular topological property of the shadow has been revealed upon studying the behavior of the topological quantity δ as a function of λ. At some critical value λ_c, we have found that there is a possible topological phase transition. In this transition, the rotating EYM BH first becomes extremal and then turns to a horizonless compact object without spacetime singularities at the center.

In addition, we have studied the connection between the real part of QNMs in the eikonal limit and the shadow radius. First, using the WKB approximation to the sixth order, we have shown that the quasinormal frequencies in the spacetime of the EYM BH deviate from those of the Schwarzschild BH; that is, $\omega_{\Re}$ increases with increasing Q. We have shown that the same result is obtained if we fix the magnetic charge Q and increase the parameter λ, although the effect is very small. This suggests that the shadow radius R_S decreases due to the inverse relation given by Eqs. (58) and (59), respectively. We have verified this result by means of the geodesic approach with the shadow images given in Figs. 6 and 7. Despite the fact the effect of λ is small, we have used the M87 black hole parameters and shown that the rotating EYM black hole can be distinguished from the Kerr-Newman black hole with a magnetic charge. The difference between the angular diameters of their shadows is given by the interval $\Delta\theta_s \in (0.11\text{–}0.61)$ μ-arc sec with $\lambda \in (0.1\text{–}0.5)$. In addition, we studied observational constraints on the EYM parameter λ via frequency analysis of QPOs and the EHT data of shadow cast by the M87 central black hole. It is interesting to note that EHT data offer tighter constraints on the parameter λ as compared to QPO's associated with microquasars.

We have also examined the dynamical evolution of the scalar and electromagnetic perturbations using the time domain integration. We have shown that the decaying rates of the scalar and electromagnetic perturbations in the rotating EYM BH are slower than that of the Schwarzschild BH and end up in a tail.

Finally, we have considered the QPOs and their resonances generated by a test particle undergoing a circular motion in the symmetric plane of the rotating EYM BH. We have employed the usually put-forward assumptions: $\nu_U = \nu_\theta$, $\nu_L = \nu_r$ with $\nu_U/\nu_L = 3/2$. With these assumptions, we have explored in details the effects of the parameter λ_0 on the frequencies of QPOs. For the uncharged rotating EYM BHs, we have shown that the value of λ_0 lies

in an interval bounded below by 0 and above by 4.3. This has allowed us to obtain good and complete curve fittings for the three microquasars GRO J1655-40, XTE J1550-564, and GRS 1915 + 105, all treated as rotating neutral EYM BHs.

ACKNOWLEDGMENTS

M. J. would like to thank Kai Lin for supporting us with numerical codes for the study of the evolution of the scalar field perturbations. S.-W. Wei is supported by National Natural Science Foundation of China (NNSFC) with the Grant No. 11675064, while A. W. is supported in part by NNSFC with the Grants No. 11675145 and No. 11975203.

APPENDIX A: EINSTEIN FIELD EQUATIONS

The nonvanishing components of the Einstein tensor are given by [11]

$$
\begin{aligned}
G_{tt} &= \frac{2\Upsilon'(a^4\cos^4\theta - a^4\cos^2\theta + a^2r^2 + r^4 - 2\Upsilon r^3)}{\Sigma^3} - \frac{a^2 r\sin^2\theta\Upsilon''}{\Sigma^3},\\
G_{rr} &= -\frac{2\Upsilon' r^2}{\Delta\Sigma},\\
G_{\theta\theta} &= -\frac{\Upsilon'' a^2 r^2\cos^2\theta + 2\Upsilon' a^2\cos^2\theta + \Upsilon'' r^3}{\Sigma},\\
G_{t\phi} &= \frac{a\sin^2\theta}{\Sigma^3}[r(a^2+r^2)\Sigma\Upsilon'' + 2\Upsilon'((a^2+r^2)a^2\cos^2\theta - a^2r^2 - r^3(r-2\Upsilon))],\\
G_{\phi\phi} &= -\frac{\sin^2\theta}{\Sigma^3}[r(a^2+r^2)^2\Sigma\Upsilon'' + 2a^2\Upsilon'(\cos^2\theta(a^4+3a^2r^2+2r^4-2\Upsilon r^3) - a^2r^2 - r^4 + 2\Upsilon r^3)].
\end{aligned}
\tag{A1}
$$

APPENDIX B: QPOs' EXPRESSIONS

In terms of x, a_0, and λ_0, the quantities N, N_r, D_r, N_θ, and D_θ appearing in (86) are given by

$$
\begin{aligned}
N = \frac{1}{[(x^4+2\lambda_0)^2 - a_0^2(x^5-6x\lambda_0)]^2}\Big[&2x^{3/2}a_0^3\sqrt{x^4-6\lambda_0}(x^8-4x^4\lambda_0-12\lambda_0^2)\\
&+2x^{7/2}a_0\sqrt{x^4-6\lambda_0}(3x^8+4x^4\lambda_0-4\lambda_0^2) + (x^4+2\lambda_0)^2(-3x^7+x^8+2x^3\lambda_0+4x^4\lambda_0+4\lambda_0^2)\\
&+a_0^2(-3x^{12}-3x^{13}+20x^8\lambda_0+6x^9\lambda_0-12x^4\lambda_0^2+60x^5\lambda_0^2+72x\lambda_0^3)\Big],
\end{aligned}
\tag{B1}
$$

$$
\begin{aligned}
N_r = {}&(x^5+2x\lambda_0)^2(-6x^7+x^8-12x^3\lambda_0+36x^4\lambda_0-60\lambda_0^2) + a_0^4(-3x^{13}+70x^9\lambda_0-324x^5\lambda_0^2+72x\lambda_0^3)\\
&+2x^{5/2}a_0\sqrt{x^4-6\lambda_0}(6x^{11}+3x^{12}+24x^7\lambda_0-46x^8\lambda_0+24x^3\lambda_0^2-92x^4\lambda_0^2+24\lambda_0^3)\\
&+a_0^2(-6x^{14}-15x^{15}-3x^{16}+24x^{10}\lambda_0+190x^{11}\lambda_0+40x^{12}\lambda_0+72x^6\lambda_0^2-468x^7\lambda_0^2+184x^8\lambda_0^2-792x^3\lambda_0^3\\
&+160x^4\lambda_0^3-48\lambda_0^4) + 2a_0^3\Big(4x^{23/2}\sqrt{x^4-6\lambda_0}+3x^{25/2}\sqrt{x^4-6\lambda_0}-48x^{15/2}\sqrt{x^4-6\lambda_0}\lambda_0\\
&-46x^{17/2}\sqrt{x^4-6\lambda_0}\lambda_0+144x^{7/2}\sqrt{x^4-6\lambda_0}\lambda_0^2-92x^{9/2}\sqrt{x^4-6\lambda_0}\lambda_0^2+24\lambda_0^3\sqrt{x^5-6x\lambda_0}\Big),
\end{aligned}
\tag{B2}
$$

$$
\begin{aligned}
D_r = x(x^4+2\lambda_0)\Big[&2x^{3/2}a_0^3\sqrt{x^4-6\lambda_0}(x^8-4x^4\lambda_0-12\lambda_0^2) + 2x^{7/2}a_0\sqrt{x^4-6\lambda_0}(3x^8+4x^4\lambda_0-4\lambda_0^2)\\
&+(x^4+2\lambda_0)^2(-3x^7+x^8+2x^3\lambda_0+4x^4\lambda_0+4\lambda_0^2) + a_0^2(-3x^{12}-3x^{13}+20x^8\lambda_0+6x^9\lambda_0-12x^4\lambda_0^2\\
&+60x^5\lambda_0^2+72x\lambda_0^3)\Big],
\end{aligned}
\tag{B3}
$$

$$N_\theta = (x^4-6\lambda_0)(x^5+2x\lambda_0)^2 - 2x^{5/2}a_0\sqrt{x^4-6\lambda_0}(3x^8+4x^4\lambda_0-4\lambda_0^2) + a_0^4(3x^9-20x^5\lambda_0+12x\lambda_0^2)$$
$$+ a_0^2(9x^{11}+3x^{12}-44x^7\lambda_0+10x^8\lambda_0-60x^3\lambda_0^2+4x^4\lambda_0^2-8\lambda_0^3) + a_0^3\Big(-4x^{15/2}\sqrt{x^4-6\lambda_0}$$
$$- 6x^{17/2}\sqrt{x^4-6\lambda_0} + 24x^{7/2}\sqrt{x^4-6\lambda_0}\lambda_0 - 8x^{9/2}\sqrt{x^4-6\lambda_0}\lambda_0 + 8\lambda_0^2\sqrt{x^5-6x\lambda_0}\Big), \tag{B4}$$

$$D_\theta = x\Big[2x^{3/2}a_0^3\sqrt{x^4-6\lambda_0}(x^8-4x^4\lambda_0-12\lambda_0^2) + 2x^{7/2}a_0\sqrt{x^4-6\lambda_0}(3x^8+4x^4\lambda_0-4\lambda_0^2) \tag{B5}$$
$$+ (x^4+2\lambda_0)^2(-3x^7+x^8+2x^3\lambda_0+4x^4\lambda_0+4\lambda_0^2) + a_0^2(-3x^{12}-3x^{13}+20x^8\lambda_0+6x^9\lambda_0-12x^4\lambda_0^2$$
$$+ 60x^5\lambda_0^2+72x\lambda_0^3)\Big]. \tag{B6}$$

[1] K. Akiyama *et al.* (Event Horizon Telescope Collaboration), Astrophys. J. **875**, L1 (2019).
[2] K. Akiyama *et al.* (Event Horizon Telescope Collaboration), Astrophys. J. **875**, L6 (2019).
[3] K. Jusufi, M. Jamil, P. Salucci, T. Zhu, and S. Haroon, Phys. Rev. D **100**, 044012 (2019).
[4] T. Zhu, Q. Wu, M. Jamil, and K. Jusufi, Phys. Rev. D **100**, 044055 (2019).
[5] S. Haroon, M. Jamil, K. Jusufi, K. Lin, and R. B. Mann, Phys. Rev. D **99**, 044015 (2019).
[6] S. Haroon, K. Jusuf, and M. Jamil, Universe **6**, 23 (2020).
[7] M. Amir, K. Jusufi, A. Banerjee, and S. Hansraj, Classical Quantum Gravity **36**, 215007 (2019).
[8] C. Bambi, K. Freese, S. Vagnozzi, and L. Visinelli, Phys. Rev. D **100**, 044057 (2019).
[9] S. Vagnozzi and L. Visinelli, Phys. Rev. D **100**, 024020 (2019).
[10] E. T. Newman, R. Couch, K. Chinnapared, A. Exton, A. Prakash, and R. Torrence, J. Math. Phys. (N.Y.) **6**, 918 (1965).
[11] M. Azreg-Aïnou, Phys. Rev. D **90**, 064041 (2014).
[12] M. Azreg-Aïnou, Phys. Lett. B **730**, 95 (2014).
[13] M. Azreg-Aïnou, Eur. Phys. J. C **74**, 2865 (2014).
[14] E. Contreras, J. M. Ramirez-Velasquez, Á. Rincón, G. Panotopoulos, and P. Bargueño, Eur. Phys. J. C **79**, 802 (2019).
[15] B. Toshmatov, Z. Stuchlík, and B. Ahmedov, Eur. Phys. J. Plus **132**, 98 (2017).
[16] A. Abdujabbarov, B. Toshmatov, Z. Stuchlík, and B. Ahmedov, Int. J. Mod. Phys. D **26**, 1750051 (2017).
[17] Z. Xu and J. Wang, Phys. Rev. D **95**, 064015 (2017).
[18] B. Toshmatov, Z. Stuchlík, and B. Ahmedov, Mod. Phys. Lett. A **32**, 1775001 (2017).
[19] S. Haroon, M. Jamil, K. Lin, P. Pavlovic, M. Sossich, and A. Wang, Eur. Phys. J. C **78**, 519 (2018).
[20] Z. Xu, X. Hou, X. Gong, and J. Wang, Eur. Phys. J. C **78**, 513 (2018).
[21] B. Toshmatov, Z. Stuchlík, and B. Ahmedov, Phys. Rev. D **95**, 084037 (2017).
[22] M. Azreg-Aïnou, Eur. Phys. J. C **76**, 3 (2016).
[23] M. Azreg-Aïnou, Eur. Phys. J. C **76**, 7 (2016).
[24] Z. Xu, X. Hou, and J. Wang, Classical Quantum Gravity **35**, 115003 (2018).
[25] C. A. Benavides-Gallego, A. A. Abdujabbarov, and C. Bambi, Phys. Rev. D **101**, 044038 (2020).
[26] M. Azreg-Aïnou, S. Haroon, M. Jamil, and M. Rizwan, Int. J. Mod. Phys. D **28**, 1950063 (2019).
[27] Z. Xu, X. Gong, and S-N. Zhang, Phys. Rev. D **101**, 024029 (2020).
[28] M. Sharif and Q. Ama-Tul-Mughani, Eur. Phys. J. Plus **134**, 616 (2019).
[29] N. Bretón, C. Lämmerzahl, and A. Macías, Classical Quantum Gravity **36**, 235022 (2019).
[30] C-Y. Chen and P. Chen, Phys. Rev. D **100**, 104054 (2019).
[31] Z. Xu, Y. Liao, and J. Wang, Int. J. Mod. Phys. A **34**, 1950185 (2019).
[32] K. Jusufi, M. Jamil, H. Chakrabarty, Q. Wu, C. Bambi, and A. Wang, Phys. Rev. D **101**, 044035 (2020).
[33] Z. Xu, M. Tang, G. Cao, and S.-N. Zhang, Eur. Phys. J. C **80**, 70 (2020).
[34] R. Kumar and S. G. Ghosh, J. Cosmol. Astropart. Phys. 07 (2020) 053.
[35] E. Contreras, Á. Rincón, G. Panotopoulos, P. Bargueño, and B. Koch, Phys. Rev. D **101**, 064053 (2020).
[36] R. Shaikh, Phys. Rev. D **100**, 024028 (2019).
[37] J. A. Smoller, A. G. Wasserman, and S. T. Yau, Commun. Math. Phys. **154**, 377 (1993).
[38] M. S. Volkov and N. Straumann, Phys. Rev. Lett. **79**, 1428 (1997).
[39] B. Kleihaus and J. Kunz, Phys. Rev. Lett. **86**, 3704 (2001).

[40] B. Kleihaus, J. Kunz, and F. Navarro-Lérida, Phys. Rev. D **66**, 104001 (2002).
[41] S. G. Ghosh and N. Dadhich, Phys. Rev. D **82**, 044038 (2010).
[42] T. Moon, Y. S. Myung, and E. J. Son, Gen. Relativ. Gravit. **43**, 3079 (2011).
[43] J. A. R. Cembranos and J. G. Valcarcel, Eur. Phys. J. C **77**, 853 (2017).
[44] M. Protter and A. DeBenedictis, Phys. Rev. D **97**, 106009 (2018).
[45] A. B. Balakin, J. P. S. Lemos, and A. E. Zayats, Phys. Rev. D **93**, 024008 (2016).
[46] A. B. Balakin and A. E. Zayats, Phys. Lett. B **644**, 294 (2007).
[47] F.-Y. Liu, Y.-F. Mai, W.-Y. Wu, and Y. Xie, Phys. Lett. B **795**, 475 (2019).
[48] R. Ibadov, B. Kleihaus, J. Kunz, and Y. Shnir, Phys. Lett. B **609**, 150 (2005).
[49] R. Ibadov, B. Kleihaus, J. Kunz, and M. Wirschins, Phys. Lett. B **627**, 180 (2005).
[50] K. Jusufi, Phys. Rev. D **101**, 124063 (2020).
[51] K. Hioki and K. I. Maeda, Phys. Rev. D **80**, 024042 (2009).
[52] S.-W. Wei, Y.-X. Liu, and R. B. Mann, Phys. Rev. D **99**, 041303 (2019).
[53] S.-W. Wei, Y.-C. Zou, Y.-X. Liu, and R. B. Mann, J. Cosmol. Astropart. Phys. 08 (2019) 030.
[54] P. Mazur and E. Mottola, Proc. Natl. Acad. Sci. U.S.A. **101**, 9545 (2004).
[55] V. Cardoso, A. S. Miranda, E. Berti, H. Witek, and V. T. Zanchin, Phys. Rev. D **79**, 064016 (2009).
[56] I. Z. Stefanov, S. S. Yazadjiev, and G. G. Gyulchev, Phys. Rev. Lett. **104**, 251103 (2010).
[57] S.-W. Wei, Y.-X. Liu, and H. Guo, Phys. Rev. D **84**, 041501 (2011).
[58] S.-W. Wei and Y.-X. Liu, Phys. Rev. D **89**, 047502 (2014).
[59] S.-W. Wei and Y.-X. Liu, Chin. Phys. C **44**, 115103 (2020).
[60] K. Jusufi, Phys. Rev. D **101**, 084055 (2020).
[61] C. Liu, T. Zhu, Q. Wu, K. Jusufi, M. Jamil, M. Azreg-Aïnou, and A. Wang, Phys. Rev. D **101**, 084001 (2020).
[62] K. Jusufi, M. Amir, M. S. Ali, and S. D. Maharaj, Phys. Rev. D **102**, 064020 (2020).
[63] B. Cuadros-Melgar, R. D. B. Fontana, and J. de Oliveira, arXiv:2005.09761.
[64] B. F. Schutz and C. M. Will, Astrophys. J. Lett. **291**, L33 (1985).
[65] S. Iyer and C. M. Will, Phys. Rev. D **35**, 3621 (1987).
[66] R. A. Konoplya, Phys. Rev. D **68**, 024018 (2003).
[67] J. Li, K. Lin, and N. Yang, Eur. Phys. J. C **75**, 131 (2015).
[68] T. E. Strohmayer, Astrophys. J. Lett. **552**, L49 (2001).
[69] J. E. McClintock, R. Narayan, S. W. Davis, L. Gou, A. Kulkarni, J. A. Orosz, R. F. Penna, R. A. Remillard, and J. F. Steiner, Classical Quantum Gravity **28**, 114009 (2011).
[70] R. Shafee, J. E. McClintock, R. Narayan, S. W. Davis, L.-X. Li, and R. A. Remillard, Astrophys. J. Lett. **636**, L113 (2006).
[71] M. A. Abramowicz, V. Karas, W. Kluźniak, W. Lee, and P. Rebusco, Publ. Astron. Soc. Jpn. **55**, 467 (2003).
[72] J. Horák and V. Karas, Astron. Astrophys. **451**, 377 (2006).
[73] A. N. Aliev and D. V. Galtsov, Gen. Relativ. Gravit. **13**, 899 (1981).
[74] M. Azreg-Aïnou, Int. J. Mod. Phys. D **28**, 1950013 (2019).
[75] L. D. Landau and E. M. Lifshitz, *Mechanics*, 3rd ed. (Pergamon Press, Oxford, 1976).
[76] A. H. Nayfeh and D. T. Mook, *Nonlinear Oscillations* (Wiley-VCH Verlag, New Jersey, 1995).
[77] A. Lindner and D. Strauch, *A Complete Course on Theoretical Physics: From Classical Mechanics to Advanced Quantum Statistics* (Springer Nature Switzerland AG, Cham, 2018).
[78] E. I. Butikov, Comput. Sci. Eng. **1**, 76 (1999).
[79] M. Kološ, Z. Stuchlík, and A. Tursunov, Classical Quantum Gravity **32**, 165009 (2015).
[80] M. Azreg-Aïnou, Z. Chen, B. Deng, M. Jamil, T. Zhu, Q. Wu, and Y.-K. Lim, Phys. Rev. D **102**, 044028 (2020).